

A Statistical MIMO Channel Model for Reconfigurable Intelligent Surface Assisted Wireless Communications

Baiping Xiong^{ID}, Zaichen Zhang^{ID}, *Senior Member, IEEE*, Hao Jiang^{ID}, *Member, IEEE*,
Hongming Zhang, *Member, IEEE*, Jiangfan Zhang^{ID}, *Member, IEEE*,
Liang Wu^{ID}, *Senior Member, IEEE*, and Jian Dang^{ID}, *Senior Member, IEEE*

Abstract—Reconfigurable intelligent surface (RIS) consisting of a large number of programmable near-passive units has been a hot topic in wireless communications due to its capability in providing smart radio environments to enhance the communication performance. However, the existing research are mainly based on simplistic channel models, which will, in principle, lead to inaccurate analysis of the system performance. In this paper, we propose a general three-dimensional (3D) wideband non-stationary end-to-end channel model for RIS assisted multiple-input multiple-output (MIMO) communications, which takes into account the physical properties of RIS, such as unit numbers, unit sizes, array orientations and array configurations. By modeling the RIS by a virtual cluster, we describe the end-to-end channel by a superposition of virtual line-of-sight (V-LoS), single-bounced non-LoS (SB-NLoS), and double-bounced NLoS (DB-NLoS) components. We also derive an equivalent cascaded channel model and show the equivalence between end-to-end and cascaded modeling of RIS channels. Then, a sub-optimal

solution with low complexity is used to derive the RIS reflection phases. The impact of physical properties of RIS, such as unit numbers, unit sizes, array orientations, array configurations and array relative locations, on channel statistical characteristics has been investigated and analyzed, the results demonstrate that the proposed model is helpful for characterizing the RIS-assisted communication channels.

Index Terms—Reconfigurable intelligent surface, MIMO, channel model, virtual cluster, statistical properties.

I. INTRODUCTION

THE deployment of fifth generation (5G) wireless communication networks is in full swing all over the world bringing various key technologies such as millimeter wave (mmWave), non-orthogonal multiple access (NOMA), and massive multiple-input multiple-output (MIMO) [1]. However, 5G seems unable to meet the increasing requirements of the future, and hence the pilot research on sixth generation (6G) wireless communications has been put on the agenda from both academia and industry [2]. Considered as a promising new technology to realize cost/energy/spectral efficient communications in 6G, reconfigurable intelligent surface (RIS) has drawn significant attentions due to its capability in providing smart and programmable radio environments to enhance the communication quality [3], [4]. RIS technology is enabled by a meta-surface consisting of a large number of independently controlled low-cost, near-passive, and subwavelength scale reflecting units with programmable electromagnetic responses such as amplitudes, phases, and polarizations, which have the ability to manipulate the impinging waves towards the destination directions constructively behaving like virtual beams from RIS to the destinations [5], [6]. For taking full advantages of RIS in communications, it is of vital importance to gain an in-depth understanding of the RIS propagation channels.

A. Related Work

Recently, there have been fast increasing research efforts on RIS assisted wireless communications. Specifically, by incorporating with RIS in indoor environments, the authors in [7] introduced the concept of programmable wireless communications. In [8], the authors shown the RIS can provide up to three times higher energy efficiency comparing to conventional

Manuscript received April 28, 2021; revised September 16, 2021; accepted November 11, 2021. Date of publication December 1, 2021; date of current version February 17, 2022. This work is supported by NSFC projects (62171127, 61960206005, 61971136, 61803211, 61871111, and 62101275), National Key R&D Program of China (2020YFB1806603), Jiangsu NSF projects (BK20191261, BK20200820, and BK20200393), the Fundamental Research Funds for the Central Universities (2242021k30043 and 2242021k30053), Research Fund of National Mobile Communications Research Laboratory, and Zhishan Youth Scholar Program of SEU. The associate editor coordinating the review of this article and approving it for publication was E. Basar. (*Corresponding authors: Zaichen Zhang; Hao Jiang.*)

Baiping Xiong is with the National Mobile Communications Research Laboratory, Frontiers Science Center for Mobile Information Communication and Security, Southeast University, Nanjing 210096, China (e-mail: xiongbp@seu.edu.cn).

Zaichen Zhang, Liang Wu, and Jian Dang are with the National Mobile Communications Research Laboratory, Frontiers Science Center for Mobile Information Communication and Security, Southeast University, Nanjing 210096, China, and also with Purple Mountain Laboratories, Nanjing 211111, China (e-mail: zczhang@seu.edu.cn; wuliang@seu.edu.cn; dangjian@seu.edu.cn).

Hao Jiang is with the College of Artificial Intelligence, Nanjing University of Information Science and Technology, Nanjing 210044, China, and also with the National Mobile Communications Research Laboratory, Frontiers Science Center for Mobile Information Communication and Security, Southeast University, Nanjing 210096, China (e-mail: jianghao@nuist.edu.cn).

Hongming Zhang is with the School of Information and Communication Engineering, Beijing University of Posts and Telecommunications, Beijing 100876, China (e-mail: zhanghm@bupt.edu.cn).

Jiangfan Zhang is with the Department of Electrical and Computer Engineering, Missouri University of Science and Technology, Rolla, MO 65409 USA (e-mail: jiangfanzhang@mst.edu).

Color versions of one or more figures in this article are available at <https://doi.org/10.1109/TCOMM.2021.3129926>.

Digital Object Identifier 10.1109/TCOMM.2021.3129926

0090-6778 © 2021 IEEE. Personal use is permitted, but republication/redistribution requires IEEE permission.

See <https://www.ieee.org/publications/rights/index.html> for more information.

multi-antenna amplify-and-forward (AF) relaying. The authors in [9] jointly optimized the transmit beamforming at the access point (AP) and reflect beamforming at the RIS to minimize the total transmit power in a multiple users multiple-input single-output (MISO) system. Then, in [10], the trajectory of the unmanned aerial vehicle (UAV) in a UAV-assisted and RIS-supported terahertz (THz) communications was optimized to maximize the average achievable rate. Moreover, performance of RIS assisted MIMO symbiotic radio networks and that of RIS assisted single-input single-output (SISO) system in near-field as well as far-field conditions were studied in [11] and [12], respectively. Apart from the above-mentioned optimizations of the beamforming matrices, performance comparisons between RIS and classic decode and forward (DF) relaying and that between RIS and AF relaying were studied in [13], [14]. Transceiver design based on RIS architectures for cost effective communications was discussed in [15]. RIS-based index modulation for achieving spectral efficient communications in the context of beyond MIMO solutions was proposed in [16]. Moreover, deep learning empowered energy efficient communications for RIS-assisted networks was studied in [17].

It should be noted that the deployment of RIS will result in significant changes of the propagation channels, thus the research efforts on RIS-assisted channels are urgently needed. The authors in [18] derived a far-field pathloss using physical optics techniques and explained how RIS reflect the impinging waves to the desired direction. The authors in [19] and [20] leveraged the physics-based approaches to characterize the path loss of the RIS component, where the far-field and near-field deployment of RIS, as well as the RIS size are considered. Moreover, by studying the physics and electromagnetic nature of RIS, free-space path loss models for far-field beamforming and near-field broadcasting scenarios were developed and verified via measurement in [21]. However, these channel models are mainly path loss models, which are generally for large-scale fading and specific communication scenarios. The authors in [22] provided a channel model for RIS aided communications under isotropic scattering assumption and showed that the transmitter-RIS and(or) RIS-receiver subchannels can be characterized by uncorrelated Rayleigh fading for linear RIS with half-wavelength spacing but not for rectangular RIS. However, the model in [22] was restricted for single-antenna system. By partitioning the large RIS into tiles, and meanwhile considering the impacts of unit number and polarization, the authors in [23] developed a statistical channel model, where the channel response is derived by incorporating the tile responses. However, the model in [23] is based on simplistic channel models and ignored the practical deployment of RIS, such as RIS orientations. The authors in [24] and [25] developed the physical statistical channel models for RIS assisted indoor and outdoor mmWave communications under SISO and MIMO scenarios, respectively. In these studies, the authors introduced the clusters in the transmitter-RIS and RIS-receiver subchannels. However, the models in [24] and [25] are restricted for narrowband stationary systems. In [26], the authors proposed a three-dimensional (3D) geometry-based stochastic model (GBSM) for a massive MIMO communi-

cation system employing RIS; however, the impacts of the physical properties of RIS is not considered. In general, the aforementioned RIS channel models simply generate the subchannel coefficients by some specific random variables, e.g., complex Gaussian random variables, and the practical deployment of RIS, especially the RIS orientation, is not well considered. They make these RIS channel models untraceable in time evolution, with poor generality to be adapted for different communication scenarios, and with low accuracy to describe the surrounding scattering environments between the transceiver. This will in principle cause inaccurate analysis of the channel statistical properties and limited scope of the models. Overall, the aforementioned channel models cannot be used to efficiently depict the realistic RIS propagation channels.

B. Motivations

Apart from large-scale path loss channels, the multipath small-scale fading of the signals also has great impacts on the RIS-assisted communication performance [27]. However, the currently available RIS channel models, such as [23] and [24], are mainly based on simplified mathematical models that generates the channel coefficients by specific distributions. These channel models while retain the statistical nature of the channel, they have poor generality and low accuracy to describe the realistic RIS-assisted propagation environments. Furthermore, the practical deployment of RIS, especially the RIS orientation, and the impact of the physical properties of RIS on channel propagation characteristics have not been sufficiently investigated in the existing literature. They motivate us to attach more importance on developing general statistical channel models to effectively characterize the realistic RIS communication channels.

C. Main Contributions

In this paper, we propose a general 3D wideband non-stationary GBSM to describe the multipath small-scale fading of the RIS-assisted MIMO communication channels. The modeling of the large-scale path loss can be referred to [18]–[21]. Overall, the main contributions and novelties of this paper are summarized as follows:

- We develop a general non-stationary 3D wideband GBSM with time-varying model parameters for characterizing the multipath small-scale fading of typical RIS assisted MIMO communication channels, which takes into account the important physical properties of RIS, such as unit number and size, relative locations among Tx, RIS, and MR, RIS configuration and orientation. The proposed GBSM can be generalized to describe various RIS-assisted communication scenarios by appropriately adjusting the model parameters.
- Unlike existing RIS channel models, the proposed GBSM models the RIS by virtual cluster and the RIS units by virtual scatterers. In this case, we express the end-to-end complex channel impulse response (CIR) between the Tx and MR as a superposition of three components, that is, the virtual line-of-sight (V-LoS) component

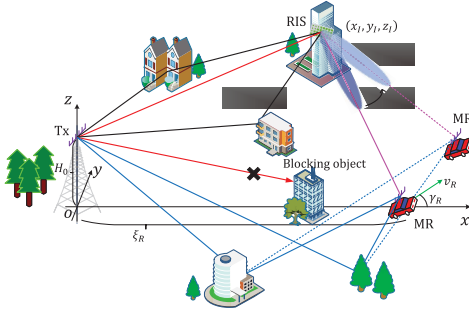


Fig. 1. A physical illustration of the proposed 3D wideband channel model for RIS assisted MIMO communications. The direct path between Tx and MR is assumed to be blocked.

through RIS, the single-bounced non-LoS (SB-NLoS) components through clusters, and the double-bounced NLoS (DB-NLoS) components through clusters and RIS, respectively.

- Based on the proposed end-to-end channel model, we derive an equivalent cascaded channel model in frequency domain, which reveals the equivalence between the end-to-end and cascaded modeling of RIS channels. Then, analytical expression of the time-varying RIS reflection phase is obtained by utilizing the generalized law of reflection [28], which provides a useful insight on how the reflection phases are affected by the model parameters.
- Based on the non-isotropic scattering assumption, the statistical properties of the proposed model including spatial cross-correlation functions (CCFs) and temporal auto-correlation functions (ACFs) are derived and analyzed. The results show that the physical properties of RIS, such as unit numbers and sizes, relative locations among Tx, RIS, and MR, RIS configurations and orientations, etc., have a great impact on channel propagation characteristics, which can be helpful for the design of RIS-assisted communication systems.

The remainder of this paper is organized as follows. In Section II, we first presents the proposed model to describe the RIS assisted wireless communication channels; then, we derive a phase shifter model to describe the phase response of the RIS. Section III derives the important statistical properties of the proposed channel model in the presence of RIS. The simulation results and discussions are presented in Section IV. Finally, Section V concludes this paper.

II. SYSTEM MODEL

Let us consider a typical MIMO communication scenario at a typical frequency band like sub-6 GHz, as shown in Fig. 1, where the direct path between the transmitter (Tx) and the mobile receiver (MR) is blocked due to the poor propagation environments, like buildings and trees, etc., and thus a RIS is introduced to enhance the communication performance. The proposed wideband model employs a GBSM-based approach to present the multipath propagation channel between the Tx and the MR, where both the Tx and MR is deployed with

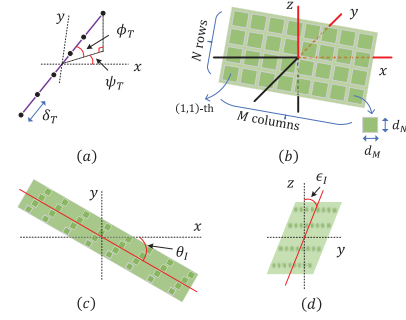


Fig. 2. Definitions of the 3D angles. (a) 3D angles of the Tx/MR ULAs, (b) 3D view of RIS, (c) horizontal rotation angle of RIS, (d) vertical rotation angle of RIS.

3D positioned omni-directional uniform linear arrays (ULAs) with antenna spacings δ_T and δ_R , respectively. The Tx ULA is placed on a static platform with an altitude of H_0 , which generally corresponds to a base station (BS), the MR ULA is moving on the ground with a speed of v_R and a direction of γ_R , and the RIS is deployed on a static platform, such as a building. Generally, it is important to take into account the ground reflection when there exists a height difference between the Tx and MR. Due to the space limitation, however, the derivations and discussions of ground reflection will be considered in our future work. Moreover, we consider that the dimensions of the Tx/MR antenna arrays and RIS are much smaller than the propagation distances, thus the planar wavefront assumption is adopted [29], [30]. In the proposed model, we define the projection of the center point of the Tx array as the origin of the coordinate system, the line connecting the origin and the center point of MR array as the x -axis, the z -axis is vertical upward, and thus the y -axis can be obtained based on the right-hand rule. It is worth mentioning that the global Cartesian coordinate system is set to be fixed during the modeling process and the model parameters are defined in this fixed global coordinate system. At the initial instant, that is $t = 0$, the center of the Tx array is located at $(0, 0, H_0)$, the center of the MR array is located at $(\xi_R, 0, 0)$, and the center of the RIS is located at (x_I, y_I, z_I) .

As is shown in Fig. 2(a), the azimuth and elevation orientation angles of the 3D positioned Tx ULA are denoted by ψ_T and ϕ_T , respectively, while at the MR, they are similarly defined and denoted by ψ_R and ϕ_R , respectively. The distance vector from the center of the Tx ULA to the p -th ($p = 1, 2, \dots, M_T$) Tx antenna and that from the center of the MR ULA to the q -th ($q = 1, 2, \dots, M_R$) MR antenna, denoted by \mathbf{A}_p^T and \mathbf{A}_q^R , respectively, can be expressed as

$$\mathbf{A}_p^T = k_p \delta_T \begin{bmatrix} \cos \phi_T \cos \psi_T \\ \cos \phi_T \sin \psi_T \\ \sin \phi_T \end{bmatrix}, \quad (1)$$

$$\mathbf{A}_q^R = k_q \delta_R \begin{bmatrix} \cos \phi_R \cos \psi_R \\ \cos \phi_R \sin \psi_R \\ \sin \phi_R \end{bmatrix}, \quad (2)$$

where $k_p = \frac{M_T - 2p + 1}{2}$ and $k_q = \frac{M_R - 2q + 1}{2}$. Let M and N denote the number of columns (counting from left to right) and

number of rows (counting from bottom to top) of the regularly arranged reflecting units in the RIS array, respectively, and let d_M and d_N denote the size of the rectangular unit along these two directions, respectively, while the unit with other shapes like triangular and circular can be considered in the future work, as is shown in Fig. 2(b). The size of the unit is usually of sub-wavelength scale, typically ranging from $1/10$ to $1/2$ of the wavelength, while the gaps between two adjacent units are generally much smaller than the dimension of the unit, and hence are ignored in the rest of the paper. It is worthy to note that the reflection-type RIS is considered in this paper, where the RIS reflects the waves in one side and no refraction occurs. The RIS channel models in existing literature, however, assume that an ideal deployment of RIS without considering the RIS orientation, which, in principle, will limit the scope of the channel models and cause inaccurate analysis of channel statistical properties. The results in [31] also imply that the RIS orientation is important in determining the RIS performance, thus also motivates us to consider the RIS orientation in RIS channel modeling. To address this limitation, we introduce a horizontal rotation angle θ_I and a vertical rotation angle ϵ_I to describe the practical orientation of the RIS surface, as shown in Fig. 2(b)-(d). This makes the proposed channel model be capable of covering a variety of practical deployments of RIS in realistic systems. Then, the distance vector from the center of the RIS to the (m, n) -th ($m = 1, 2, \dots, M; n = 1, 2, \dots, N$) RIS unit can be expressed as

$$\mathbf{A}_{mn}^{\text{RIS}} = \begin{bmatrix} k_m d_M \cos \theta_I + k_n d_N \sin \theta_I \sin \epsilon_I \\ k_m d_M \sin \theta_I - k_n d_N \cos \theta_I \sin \epsilon_I \\ k_n d_N \cos \epsilon_I \end{bmatrix}, \quad (3)$$

where $k_m = \frac{2m-M-1}{2}$ and $k_n = \frac{2n-N-1}{2}$. It is worth mentioning that the orientations of the Tx/MR ULAs are assumed to be fixed, while the orientation of the RIS can be changed by varying the rotational angles θ_I and ϵ_I to meet the requirements in different communication conditions. For example, by adjusting the horizontal rotation angle θ_I , the RIS is able to support terrestrial communications in another direction. Furthermore, by adjusting the vertical rotation angle ϵ_I , the RIS can be used to support air-to-air communications. In this paper, we will focus on investigating the impact of different orientations of RIS on channel statistical characteristics, the optimization of θ_I and ϵ_I for achieving better performance is out of the scope of this work and will be considered as a future work.

In this paper, the cluster structure is adopted to describe the multipath scattering environments between the Tx and MR, where each cluster consisting of many scatterers accounts for a distinguishable path with resolvable delay, while the scatterers in the same cluster approximately have the same distances and hence result in indistinguishable rays with unresolvable delays [32]. In the proposed wideband channel model, we assume that there are L_1 clusters forming a cluster set C^{L_1} between the Tx and MR, in which the ℓ_1 -th ($\ell_1 = 1, 2, \dots, L_1$) cluster is denoted by S_{ℓ_1} ; meanwhile, there are L_2 clusters forming a cluster set C^{L_2} between the Tx and RIS, in which the ℓ_2 -th ($\ell_2 = 1, 2, \dots, L_2$) cluster is denoted

by S_{ℓ_2} . Moreover, we adopt the uncorrelated scattering (US) assumption, which assumes all clusters to be uncorrelated, and we assume there are no shared clusters between cluster sets C^{L_1} and C^{L_2} [27]. It is worth mentioning that the waves transmitted from the Tx experience LoS and multipath NLoS propagations before arriving at the RIS. The RIS controller programs the phase shifts of the RIS units to manipulate the incident waves, the waves from both the LoS and multipath NLoS propagations, with controllable phase shifts so that the reflected waves are combined constructively at the MR, providing a narrow beam (LoS propagation) from the RIS towards the MR. Therefore, we introduce the cluster set C^{L_2} to describe the multipath scattering environment for the propagations between Tx and RIS, whereas no cluster reflection exists between RIS and MR. During the propagation, the signal impinges on the RIS units, from the Tx directly or from the clusters; then, an additional amplitude $\chi_{mn}(t)$ and phase $\varphi_{mn}(t)$ is attached during the interaction. This is similar to the signal being reflected by the scatterers, the major difference is that the reflection coefficient of the RIS unit is programmable and deterministic while that of the scatterers is random. Note that in this paper we consider the phase-shift profile of each RIS unit to be a continuous function, thus the reflection phase of the RIS units is continuous [21]. In light of this, we model the RIS array by a *virtual cluster* and the RIS units by *virtual scatterers*, which means the rays from the same source (either Tx or cluster) to the MR via different RIS units have approximately equal propagation distances and hence are indistinct. Therefore, the waves transmitted by the Tx experience three different propagation mechanisms before arriving at the MR. One is that the waves transmitted by Tx experience the reflection of the clusters in cluster set C^{L_1} before arriving at the MR without interacting with the RIS, that is, $\text{Tx} \rightarrow C^{L_1} \rightarrow \text{MR}$; the other is that the waves transmitted by Tx impinge on the RIS and then being reflected towards the MR, which is generally called the *virtual LoS component* provided by RIS [3], that is, $\text{Tx} \rightarrow \text{RIS} \rightarrow \text{MR}$; and another is that the waves transmitted by Tx experience the reflection of the clusters in cluster set C^{L_2} , and then the scattered waves are further manipulated by the RIS before arriving at the MR, that is, $\text{Tx} \rightarrow C^{L_2} \rightarrow \text{RIS} \rightarrow \text{MR}$.

A. Complex Channel Impulse Response

The underlying physical propagation properties of the proposed MIMO channel model can be characterized by a complex matrix of size $M_R \times M_T$, that is, $\mathbf{H}(t, \tau) = [h_{pq}(t, \tau)]_{M_R \times M_T}$, where $h_{pq}(t, \tau)$ denotes the complex CIR between the p -th transmitting antenna and the q -th receiving antenna, t indicates moving time and accounts for the time-varying property of the model, and τ stands for the path delay from the Tx to the MR. Furthermore, $h_{pq}(t, \tau)$ can be expressed as a summation of the V-LoS, SB-NLoS, and DB-NLoS components, that is, [32], [33]

$$h_{pq}(t, \tau) = h_{pq}^{\text{V-LoS}}(t, \tau) + h_{pq}^{\text{SB-NLoS}}(t, \tau) + h_{pq}^{\text{DB-NLoS}}(t, \tau), \quad (4)$$

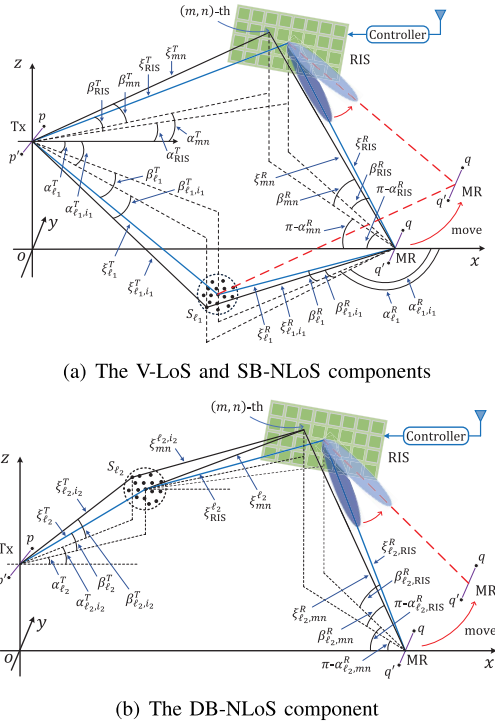


Fig. 3. A visualized illustration of the proposed 3D wideband channel model for RIS-assisted MIMO communications. For clarify, only the cluster S_{l_1} in cluster set C^{L_1} and cluster S_{l_2} in cluster set C^{L_2} are shown.

where the superscripts $[\cdot]^{V\text{-LoS}}$, $[\cdot]^{SB\text{-NLoS}}$, and $[\cdot]^{DB\text{-NLoS}}$ refer to the links of $\text{Tx} \rightarrow \text{RIS} \rightarrow \text{MR}$, $\text{Tx} \rightarrow C^{L_1} \rightarrow \text{MR}$, and $\text{Tx} \rightarrow C^{L_2} \rightarrow \text{RIS} \rightarrow \text{MR}$, respectively. Fig. 3 illustrates the definitions of the key model parameters of the V-LoS, SB-NLoS, and DB-NLoS components at the initial instant, respectively, the definitions of the parameters at the real-time stage are the same and are omitted here. It is worth mentioning that in the proposed model only the motion of the MR is considered, and hence the model parameters at the MR side is time-varying.

1) *V-LoS Component* $h_{pq}^{V\text{-LoS}}(t, \tau)$: One of the fascinating benefits of RIS lies in its ability to provide a *physical indirect but deterministic* link between the Tx and MR to enhance the communications when the physical LoS path between them is blocked. The SB-NLoS and DB-NLoS components, that is, $h_{pq}^{SB\text{-NLoS}}(t, \tau)$ and $h_{pq}^{DB\text{-NLoS}}(t, \tau)$, on the other hand, are random processes. Therefore, we can similarly introduce a factor $K_{\text{Rice}}^{\text{vir}}$ to denote the power ratio between the deterministic (V-LoS) and random (SB-NLoS and DB-NLoS) components [34]. Then, the V-LoS component $h_{pq}^{V\text{-LoS}}(t, \tau)$ can be expressed as

$$h_{pq}^{V\text{-LoS}}(t, \tau) = \sqrt{\frac{K_{\text{Rice}}^{\text{vir}}}{K_{\text{Rice}}^{\text{vir}} + 1}} \times \sum_{m=1}^M \sum_{n=1}^N \frac{1}{\sqrt{MN}} \chi_{mn}(t) e^{j(\varphi_{mn}(t) - \frac{2\pi}{\lambda}(\xi_{mn}^{T,p} + \xi_{mn}^{R,q}(t)))} \times e^{j\frac{2\pi}{\lambda}v_R t \cos(\alpha_{mn}^R(t) - \gamma_R) \cos \beta_{mn}^R(t)} \delta(\tau - \tau^{V\text{-LoS}}(t)), \quad (5)$$

where λ is the carrier wavelength, $\tau^{V\text{-LoS}} = (\xi_{\text{RIS}}^T + \xi_{\text{RIS}}^R(t))/c$ denotes the propagation delay of the waves from the center

of the Tx array to that of the MR array via the center of the RIS, ξ_{RIS}^T and $\xi_{\text{RIS}}^R(t)$ are the distance between the centers of the RIS and Tx array and that between the centers of the RIS and MR array, respectively, and $c = 3.0 \times 10^8$ m/s is the speed of light. Distances $\xi_{mn}^{T,p}$ and $\xi_{mn}^{R,q}(t)$ are the propagation distances from the p -th transmitting antenna and q -th receiving antenna to the (m, n) -th RIS unit, respectively. Moreover, symbols $\alpha_{mn}(t)$ and $\beta_{mn}(t)$ denote the azimuth angle of arrival (AAoA) and elevation angle of arrival (EAoA) of the waves experiencing the V-LoS link from the (m, n) -th RIS unit to the MR, respectively. The corresponding azimuth angle of departure (AAoD) and elevation angle of departure (EAoD) of the V-LoS link from Tx array to the (m, n) -th RIS unit are denoted by α_{mn}^T and β_{mn}^T , respectively, which are not described explicitly in (5). It is worth mentioning that in this paper the reflecting coefficients of the RIS, that is, $\chi_{mn}(t)e^{j\varphi_{mn}(t)}$, is time-varying because of the motion of the MR. The RIS controller will perform real-time configuration of $\chi_{mn}(t)e^{j\varphi_{mn}(t)}$ to ensure the reflected beam pointing towards the MR so that the communication performance is optimized.

2) *SB-NLoS Component* $h_{pq}^{SB\text{-NLoS}}(t, \tau)$: The SB-NLoS link, that is, $\text{Tx} \rightarrow C^{L_1} \rightarrow \text{MR}$, describes the wideband multipath channel between the Tx and MR that is independent of the RIS, where each cluster in cluster set C^{L_1} contributes to a distinguishable path with resolvable delay. The modeling of the SB-NLoS component $h_{pq}^{SB\text{-NLoS}}(t, \tau)$ is similar to the modeling of conventional no-RIS wideband multipath channels [35]–[37]. Therefore, the complex CIR of the SB-NLoS component between the p -th transmitting antenna and the q -th receiving antenna can be expressed as

$$h_{pq}^{SB\text{-NLoS}}(t, \tau) = \sqrt{\frac{\eta_{\text{SB}}}{K_{\text{Rice}}^{\text{vir}} + 1}} \times \sum_{l_1=1}^{L_1} \sum_{i_1=1}^{I_1} \sqrt{\frac{P_{l_1}}{I_1}} e^{j(\varphi_{l_1, i_1} - \frac{2\pi}{\lambda}(\xi_{l_1, i_1}^{T,p} + \xi_{l_1, i_1}^{R,q}(t)))} \times e^{j\frac{2\pi}{\lambda}v_R t \cos(\alpha_{l_1, i_1}^R(t) - \gamma_R) \cos \beta_{l_1, i_1}^R(t)} \delta(\tau - \tau_{l_1}(t)), \quad (6)$$

where the weight factor η_{SB} specifies the power contribution of the SB-NLoS component to the total scattered power of the NLoS components (SB-NLoS and DB-NLoS), I_1 is the number of rays in cluster S_{l_1} , which is generally assumed to be a very large number approaching infinity, and P_{l_1} denotes the cluster power, which is normalized to satisfy $\sum_{l_1=1}^{L_1} P_{l_1} = 1$ [37]. Moreover, $\tau_{l_1}(t)$ is the propagation delay of the SB-NLoS path $\text{Tx} \rightarrow S_{l_1} \rightarrow \text{MR}$ via cluster S_{l_1} , which can be expressed as $\tau_{l_1}(t) = (\xi_{l_1}^T + \xi_{l_1}^R(t))/c$, where $\xi_{l_1}^T$ and $\xi_{l_1}^R(t)$ denote the distances from the centers of the Tx and MR arrays to cluster S_{l_1} , respectively. The distances $\xi_{l_1, i_1}^{T,p}$ and $\xi_{l_1, i_1}^{R,q}(t)$ describe the propagation distances from the p -th transmitting and q -th receiving antennas to cluster S_{l_1} via the i_1 -th ray, respectively, and $\alpha_{l_1, i_1}^R(t)$ and $\beta_{l_1, i_1}^R(t)$ represent the AAoA and EAoA of the waves scattered from cluster S_{l_1} to MR via the i_1 -th ray, respectively. In addition, the AAoD and EAoD of the SB-NLoS link from Tx to cluster S_{l_1} via the i_1 -th ray are denoted by α_{l_1, i_1}^T and β_{l_1, i_1}^T , respectively, as defined in

Fig. 3(a). Finally, φ_{ℓ_1, i_1} for $i_1 = 1, 2, \dots, I_1$ are independent and uniformly distributed random phases in the interval from $-\pi$ to π , i.e., $\varphi_{\ell_1, i_1} \sim \mathcal{U}[-\pi, \pi]$.

3) *DB-NLoS Component* $h_{pq}^{\text{DB-NLoS}}(t, \tau)$: The DB-NLoS link, that is, $\text{Tx} \rightarrow C^{L_2} \rightarrow \text{RIS} \rightarrow \text{MR}$, characterizes the multipath propagations from the Tx to the MR via double-bounced reflections, where the clusters in cluster set C^{L_2} result in the first bounce and RIS accounts for the second bounce. Owing to the assumption that the clusters in cluster set C^{L_2} are uncorrelated and different clusters can result in different distinguishable paths with resolvable delays, the DB-NLoS link $h_{pq}^{\text{DB-NLoS}}(t, \tau)$ is also a wideband component. Therefore, the complex envelop of the DB-NLoS link from the p -th transmitting antenna to the q -th receiving antenna, denoted by $h_{pq}^{\text{DB-NLoS}}(t, \tau)$, can be expressed as

$$\begin{aligned} h_{pq}^{\text{DB-NLoS}}(t, \tau) &= \sqrt{\frac{\eta_{\text{DB}}}{K_{\text{Rice}}^{\text{vir}} + 1}} \\ &\times \sum_{\ell_2=1}^{L_2} \sum_{i_2=1}^{I_2} \sqrt{\frac{P_{\ell_2}}{I_2}} \sum_{m=1}^M \sum_{n=1}^N \frac{1}{\sqrt{MN}} \chi_{mn}(t) e^{j\varphi_{mn}(t)} \\ &\times e^{j\left(\varphi_{\ell_2, i_2} - \frac{2\pi}{\lambda} \left(\xi_{\ell_2, i_2}^{T, p} + \xi_{mn}^{\ell_2, i_2} + \xi_{mn}^{R, q}(t) \right) \right)} \\ &\times e^{j\frac{2\pi}{\lambda} v_R t \cos(\alpha_{\ell_2, mn}^R(t) - \gamma_R) \cos \beta_{\ell_2, mn}^R(t) \delta(\tau - \tau_{\ell_2}^{\text{RIS}}(t))}, \end{aligned} \quad (7)$$

where η_{DB} is the weight factor that specifies the power contribution of the DB-NLoS component to the total scattered power of the NLoS components (SB-NLoS and DB-NLoS), I_2 denotes the number of rays in cluster S_{ℓ_2} , which is generally assumed to be a very large number approaching infinity, that is, $I_2 \rightarrow \infty$, and P_{ℓ_2} is the cluster power, which is normalized to satisfy $\sum_{\ell_2=1}^{L_2} P_{\ell_2} = 1$ [37]. It should be noted that the weight factors η_{SB} in (6) and η_{DB} in (7) meet with the constraint of $\eta_{\text{SB}} + \eta_{\text{DB}} = 1$, thus the total received power of $h_{pq}(t, \tau)$ is normalized to one. Moreover, $\tau_{\ell_2}^{\text{RIS}}(t)$ denotes the path delay of the DB-NLoS path $\text{Tx} \rightarrow S_{\ell_2} \rightarrow \text{RIS} \rightarrow \text{MR}$ with cluster S_{ℓ_2} as the first bounce cluster, and can be calculated by $\tau_{\ell_2}^{\text{RIS}}(t) = (\xi_{\ell_2}^T + \xi_{\text{RIS}}^R + \xi_{\ell_2, \text{RIS}}^R(t))/c$, where $\xi_{\ell_2}^T$, ξ_{RIS}^R , and $\xi_{\ell_2, \text{RIS}}^R(t)$ represent the distance between the center of Tx array and cluster S_{ℓ_2} , distance between cluster S_{ℓ_2} and the center of RIS, and distance between the centers of RIS and MR array, respectively. In addition, distances $\xi_{\ell_2, i_2}^{T, p}$, $\xi_{mn}^{\ell_2, i_2}$, and $\xi_{mn}^{R, q}(t)$ denote the propagation distance from the p -th transmitting antenna to the cluster S_{ℓ_2} via the i_2 -th ray, propagation distance from cluster S_{ℓ_2} to the (m, n) -th RIS unit via the i_2 -th ray, and propagation distance from the (m, n) -th RIS unit to the q -th receiving antenna with cluster S_{ℓ_2} as the first-bounce cluster, respectively. Furthermore, symbols $\alpha_{\ell_2, mn}^R(t)$ and $\beta_{\ell_2, mn}^R(t)$ are the AAoA and EAoA from the (m, n) -th RIS unit to the MR array with cluster S_{ℓ_2} as the first-bounce cluster, respectively. The corresponding AAoD and EAoD from Tx array to cluster S_{ℓ_2} via the i_2 -th ray, on the other hand, are denoted by α_{ℓ_2, i_2}^T and β_{ℓ_2, i_2}^T , respectively, as defined in Fig. 3(b). Finally, phases φ_{ℓ_2, i_2} for $i_2 = 1, 2, \dots, I_2$ are independent and uniformly distributed random variables in the interval $[-\pi, \pi)$, that is, $\varphi_{\ell_2, i_2} \sim \mathcal{U}[-\pi, \pi)$. It is worth

mentioning that the model in [38] employed the twin-cluster structure to describe the double bounce propagation of the signals, where the propagation between the first and last bounces is visualized to be random. In this paper, however, the propagation between the clusters in cluster set C^{L_2} and RIS is deterministic, and there is only one last bounce cluster, that is, the RIS, which is a specific feature of the RIS channel.

B. Calculation of the Model Parameters

1) *V-LoS Component* $h_{pq}^{\text{V-LoS}}(t, \tau)$: In RIS-assisted communications, once the deployment of Tx, RIS, and MR are confirmed, the V-LoS component from Tx to the MR via the reflection of RIS can be subsequently determined. Consequently, the model parameters of the V-LoS link can be derived based on the geometrical relationship and the moving time/speed/direction of the MR. Owing to the fact that the Tx and RIS are assumed to be static in this paper, the model parameters of the propagation from Tx to RIS are constant values. The distance ξ_{RIS}^T can be expressed as $\xi_{\text{RIS}}^T = \sqrt{x_I^2 + y_I^2 + (z_I - H_0)^2}$, and distance $\xi_{mn}^{T, p}$ can be calculated by $\xi_{mn}^{T, p} = \|\mathbf{d}_{\text{RIS}}^{\text{MT}} + \mathbf{A}_{mn}^{\text{RIS}} - \mathbf{A}_p^T\|$, where $\mathbf{d}_{\text{RIS}}^{\text{MT}} = [x_I, y_I, z_I - H_0]^T$ is the distance vector from the center of the Tx array to that of the RIS and $\|\cdot\|$ stands for the Frobenius norm. Moreover, the AAoD and EAoD of the V-LoS link, that is, α_{mn}^T and β_{mn}^T , respectively, can be calculated similarly by applying geometrical principles, the results are omitted here for brevity.

After a time interval of t , the moving displacement of the MR, denoted by $\Delta \mathbf{d}_{\text{MR}}(t)$, can be expressed as

$$\Delta \mathbf{d}_{\text{MR}}(t) = \begin{bmatrix} v_R t \cos \gamma_R \\ v_R t \sin \gamma_R \\ 0 \end{bmatrix}. \quad (8)$$

The distance vector from the center of the MR array to that of the RIS, at the initial instant, can be expressed as $\mathbf{d}_{\text{RIS}}^{\text{MR}}(0) = [x_I - \xi_R, y_I, z_I]^T$, where the superscript $[\cdot]^T$ denotes the transpose operator. Then, the time-varying distance vector from the center of MR array to that of the RIS can be expressed as

$$\mathbf{d}_{\text{RIS}}^{\text{MR}}(t) = \mathbf{d}_{\text{RIS}}^{\text{MR}}(0) - \Delta \mathbf{d}_{\text{MR}}(t). \quad (9)$$

Therefore, the time-varying distance $\xi_{\text{RIS}}^R(t)$ can be obtained by applying Frobenius norm to (9), that is, $\xi_{\text{RIS}}^R(t) = \|\mathbf{d}_{\text{RIS}}^{\text{MR}}(t)\|$. Moreover, the time-varying distance vector from the center of the MR array to the (m, n) -th RIS unit and that from the q -th receiving antenna to the (m, n) -th RIS unit, denoted by $\mathbf{d}_{mn}^R(t)$ and $\mathbf{d}_{mn}^{R, q}(t)$, respectively, can be expressed as

$$\mathbf{d}_{mn}^R(t) = \mathbf{d}_{\text{RIS}}^{\text{MR}}(0) + \mathbf{A}_{mn}^{\text{RIS}} - \Delta \mathbf{d}_{\text{MR}}(t), \quad (10)$$

$$\mathbf{d}_{mn}^{R, q}(t) = \mathbf{d}_{\text{RIS}}^{\text{MR}}(0) + \mathbf{A}_{mn}^{\text{RIS}} - \mathbf{A}_q^R - \Delta \mathbf{d}_{\text{MR}}(t). \quad (11)$$

Then, the propagation distance $\xi_{mn}^{R, q}(t)$ can be obtained as $\xi_{mn}^{R, q}(t) = \|\mathbf{d}_{mn}^{R, q}(t)\|$. Moreover, from (10) we can further derive the time-varying AAoA and EAoA of the V-LoS link, that is, $\alpha_{mn}^R(t)$ and $\beta_{mn}^R(t)$, respectively, which can be

expressed as [39]

$$\alpha_{mn}^R(t) = \arccos \left\{ (x_I - \xi_R + k_m d_M \cos \theta_I + k_n d_N \sin \theta_I \sin \epsilon_I - v_R t \cos \gamma_R) / \sqrt{Q_1(t)} \right\}, \quad (12)$$

$$\beta_{mn}^R(t) = \arcsin \left\{ (z_I + k_n d_N \cos \epsilon_I) / \sqrt{Q_2(t)} \right\}, \quad (13)$$

where $Q_1(t) = (x_I - \xi_R + k_m d_M \cos \theta_I + k_n d_N \sin \theta_I \sin \epsilon_I - v_R t \cos \gamma_R)^2 + (y_I + k_m d_M \sin \theta_I - k_n d_N \cos \theta_I \sin \epsilon_I - v_R t \sin \gamma_R)^2$ and $Q_2(t) = Q_1(t) + (z_I + k_n d_N \cos \epsilon_I)^2$.

2) *SB-NLoS Component* $h_{pq}^{SB-NLoS}(t, \tau)$: It should be noted that in cluster structure, the scatterers within the same cluster are generally assumed to be approximately at the same distance from the center of the Tx array but with a certain angular spread, i.e., $\xi_{\ell_1}^T \approx \xi_{\ell_1, i_1}^T \dots \approx \xi_{\ell_1, I_1}^T$ [40]. Let $\alpha_{\ell_1}^T$ and $\beta_{\ell_1}^T$ denote the mean AAoD and EAoD of the SB-NLoS link from the center of the Tx array to cluster S_{ℓ_1} , respectively. Then, the distance vector from the center of the Tx array to cluster S_{ℓ_1} can be expressed as $\mathbf{d}_{\ell_1}^T = \xi_{\ell_1}^T [\cos \beta_{\ell_1}^T \cos \alpha_{\ell_1}^T, \cos \beta_{\ell_1}^T \sin \alpha_{\ell_1}^T, \sin \beta_{\ell_1}^T]^T$, and the distance vector from the center of the Tx array to cluster S_{ℓ_1} via the i_1 -th ray, denoted by $\mathbf{d}_{\ell_1, i_1}^T$, can be expressed as $\mathbf{d}_{\ell_1, i_1}^T = \xi_{\ell_1}^T [\cos \beta_{\ell_1, i_1}^T \cos \alpha_{\ell_1, i_1}^T, \cos \beta_{\ell_1, i_1}^T \sin \alpha_{\ell_1, i_1}^T, \sin \beta_{\ell_1, i_1}^T]^T$. Therefore, the propagation distance from the p -th transmitting antenna to the cluster S_{ℓ_1} via the i_1 -th ray can be expressed as $\xi_{\ell_1, i_1}^{T, p} = \|\mathbf{d}_{\ell_1, i_1}^T - \mathbf{A}_p^T\|$. It is worth mentioning that in SB-NLoS component, the AAoD (EAoD) of the ray is related to the AAoA (EAoA) of the ray within the same cluster and this relationship can be uniquely determined by exploiting geometrical relationship. Consequently, the time-varying distance vector from the center of MR array to cluster S_{ℓ_1} , distance vector from the center of MR array to cluster S_{ℓ_1} via the i_1 -th ray, and that from the q -th receiving antenna to cluster S_{ℓ_1} via the i_1 -th ray, denoted by $\mathbf{d}_{\ell_1}^R(t)$, $\mathbf{d}_{\ell_1, i_1}^R(t)$, and $\mathbf{d}_{\ell_1, i_1}^{R, q}(t)$, respectively, can be expressed as

$$\mathbf{d}_{\ell_1}^R(t) = \mathbf{d}_{\ell_1}^T - \mathbf{d}_{MR}^{Tx} - \Delta \mathbf{d}_{MR}(t), \quad (14)$$

$$\mathbf{d}_{\ell_1, i_1}^R(t) = \mathbf{d}_{\ell_1, i_1}^T - \mathbf{d}_{MR}^{Tx} - \Delta \mathbf{d}_{MR}(t), \quad (15)$$

$$\mathbf{d}_{\ell_1, i_1}^{R, q}(t) = \mathbf{d}_{\ell_1, i_1}^T - \mathbf{d}_{MR}^{Tx} - \mathbf{A}_q^R - \Delta \mathbf{d}_{MR}(t), \quad (16)$$

where $\mathbf{d}_{MR}^{Tx} = [\xi_R, 0, -H_0]^T$ represents the distance vector from the center of Tx to that of MR array. Therefore, we can obtain $\xi_{\ell_1}^R(t) = \|\mathbf{d}_{\ell_1}^R(t)\|$ and $\xi_{\ell_1, i_1}^{R, q}(t) = \|\mathbf{d}_{\ell_1, i_1}^{R, q}(t)\|$, respectively. Moreover, the time-varying AAoA ($\alpha_{\ell_1, i_1}^R(t)$) and EAoA ($\beta_{\ell_1, i_1}^R(t)$) of the SB-NLoS link travelling via the i_1 -th ray in cluster S_{ℓ_1} can be obtained based on (15), which can be expressed as

$$\alpha_{\ell_1, i_1}^R(t) = \arcsin \frac{\xi_{\ell_1}^T \cos \beta_{\ell_1, i_1}^T \sin \alpha_{\ell_1, i_1}^T - v_R t \sin \gamma_R}{\sqrt{Q_3(t)}}, \quad (17)$$

$$\beta_{\ell_1, i_1}^R(t) = \arcsin \left\{ (\xi_{\ell_1}^T \sin \beta_{\ell_1, i_1}^T + H_0) / \sqrt{Q_4(t)} \right\}, \quad (18)$$

where $Q_3(t) = (\xi_{\ell_1}^T \cos \beta_{\ell_1, i_1}^T \cos \alpha_{\ell_1, i_1}^T - \xi_R - v_R t \cos \gamma_R)^2 + (\xi_{\ell_1}^T \cos \beta_{\ell_1, i_1}^T \sin \alpha_{\ell_1, i_1}^T - v_R t \sin \gamma_R)^2$ and $Q_4(t) = Q_3(t) + (\xi_{\ell_1}^T \sin \beta_{\ell_1, i_1}^T + H_0)^2$.

3) *DB-NLoS Component* $h_{pq}^{DB-NLoS}(t, \tau)$: In DB-NLoS link the first-bounce propagation is from Tx to the clusters in cluster set C^{L_2} . Let us take the cluster S_{ℓ_2} as an example, that is, the path of Tx $\rightarrow S_{\ell_2} \rightarrow$ RIS \rightarrow MR. Then, the distance vector from the center of the Tx array to cluster S_{ℓ_2} and that from the center of the Tx array to cluster S_{ℓ_2} via the i_2 -th ray can be expressed as $\mathbf{d}_{\ell_2}^T = \xi_{\ell_2}^T [\cos \beta_{\ell_2}^T \cos \alpha_{\ell_2}^T, \cos \beta_{\ell_2}^T \sin \alpha_{\ell_2}^T, \sin \beta_{\ell_2}^T]^T$ and $\mathbf{d}_{\ell_2, i_2}^T = \xi_{\ell_2}^T [\cos \beta_{\ell_2, i_2}^T \cos \alpha_{\ell_2, i_2}^T, \cos \beta_{\ell_2, i_2}^T \sin \alpha_{\ell_2, i_2}^T, \sin \beta_{\ell_2, i_2}^T]^T$, respectively, where $\alpha_{\ell_2}^T$ and $\beta_{\ell_2}^T$ represent the mean AAoD and EAoD between the center of Tx array and cluster S_{ℓ_2} , respectively. Then, the propagation distance from the p -th transmitting antenna to cluster S_{ℓ_2} via the i_2 -th ray can be expressed as $\xi_{\ell_2, i_2}^{T, p} = \|\mathbf{d}_{\ell_2, i_2}^T - \mathbf{A}_p^T\|$. Moreover, the distance vector from cluster S_{ℓ_2} to the center of RIS and that from cluster S_{ℓ_2} to the (m, n) -th RIS unit via the i_2 -th ray, that is, $\mathbf{d}_{RIS}^{\ell_2}$ and $\mathbf{d}_{mn}^{\ell_2, i_2}$, respectively, can be expressed as

$$\mathbf{d}_{RIS}^{\ell_2} = \mathbf{d}_{RIS}^{MT} - \mathbf{d}_{\ell_2}^T, \quad (19)$$

$$\mathbf{d}_{mn}^{\ell_2, i_2} = \mathbf{d}_{RIS}^{MT} + \mathbf{d}_{mn}^{RIS} - \mathbf{d}_{\ell_2, i_2}^T, \quad (20)$$

Therefore, the propagation distances $\xi_{RIS}^{\ell_2}$ and $\xi_{mn}^{\ell_2, i_2}$ can be obtained as $\xi_{RIS}^{\ell_2} = \|\mathbf{d}_{RIS}^{\ell_2}\|$ and $\xi_{mn}^{\ell_2, i_2} = \|\mathbf{d}_{mn}^{\ell_2, i_2}\|$, respectively.

Owing to the fact that the last-bounce propagation of the DB-NLoS link in RIS channel is the same, that is, the propagation from RIS to the MR, the model parameters (distances and angular parameters) of the sub-link from RIS to MR with different first-bounce clusters are the same, i.e., $\xi_{\ell_2=1, RIS}^R(t) = \xi_{\ell_2=2, RIS}^R(t) \dots = \xi_{\ell_2=L_2, RIS}^R(t)$, $\xi_{\ell_2=1, mn}^{R, q}(t) = \xi_{\ell_2=2, mn}^{R, q}(t) \dots = \xi_{\ell_2=L_2, mn}^{R, q}(t)$, $\alpha_{\ell_2=1, RIS}^R(t) = \alpha_{\ell_2=2, RIS}^R(t) \dots = \alpha_{\ell_2=L_2, RIS}^R(t)$, and $\beta_{\ell_2=1, RIS}^R(t) = \beta_{\ell_2=2, RIS}^R(t) \dots = \beta_{\ell_2=L_2, RIS}^R(t)$. Moreover, the DB-NLoS component $h_{pq}^{DB-NLoS}(t, \tau)$ shares the same sub-link from RIS to the MR as the V-LoS component $h_{pq}^{V-LoS}(t, \tau)$, and hence the model parameters of the sub-link from RIS to MR of the DB-NLoS component are the same as those of the V-LoS component, which means that $\xi_{\ell_2, RIS}^R(t) = \xi_{RIS}^R(t)$, $\xi_{\ell_2, mn}^{R, q}(t) = \xi_{mn}^{R, q}(t)$, $\alpha_{\ell_2, RIS}^R(t) = \alpha_{RIS}^R(t)$, and $\beta_{\ell_2, RIS}^R(t) = \beta_{RIS}^R(t)$. It is worth mentioning that the model parameters of the V-LoS component can be obtained from sub-section II.B-1).

C. Generation of the Proposed Channel Model in Frequency Domain

To make the proposed model more applicable, it is important to provide the frequency domain expression of the model and take into account the phase response of the RIS units. By applying Fourier transform to the complex CIRs $h_{pq}(t, \tau)$ with respect to delay τ , the time-varying transfer function of the proposed channel model can be expressed as [32]

$$\begin{aligned} H_{pq}(t, f) &= \int_{\tau=0}^{\infty} h_{pq}(t, \tau) e^{-j2\pi f \tau} d\tau \\ &= H_{pq}^{V-LoS}(t, f) + H_{pq}^{SB-NLoS}(t, f) + H_{pq}^{DB-NLoS}(t, f), \end{aligned} \quad (21)$$

where $H_{pq}^{V-LoS}(t, f)$, $H_{pq}^{SB-NLoS}(t, f)$, and $H_{pq}^{DB-NLoS}(t, f)$ are the transfer functions of the V-LoS, SB-NLoS, and DB-NLoS

components, respectively, which can be further expressed as

$$H_{pq}^{\text{V-LoS}}(t, f) = \sqrt{\frac{K_{\text{Rice}}^{\text{vir}}}{K_{\text{Rice}}^{\text{vir}} + 1}} \times \sum_{m=1}^M \sum_{n=1}^N \frac{1}{\sqrt{MN}} \chi_{mn}(t) e^{j(\varphi_{mn}(t) - \frac{2\pi}{\lambda} (\xi_{mn}^{T,p} + \xi_{mn}^{R,q}(t)))} \times e^{j\frac{2\pi}{\lambda} v_R t \cos(\alpha_{mn}^R(t) - \gamma_R) \cos \beta_{mn}^R(t)} e^{-j2\pi f \tau^{\text{V-LoS}}(t)}, \quad (22)$$

$$H_{pq}^{\text{SB-NLoS}}(t, f) = \sqrt{\frac{\eta_{\text{SB}}}{K_{\text{Rice}}^{\text{vir}} + 1}} \times \sum_{\ell_1=1}^{L_1} \sum_{i_1=1}^{I_1} \sqrt{\frac{P_{\ell_1}}{I_1}} e^{j(\varphi_{\ell_1, i_1} - \frac{2\pi}{\lambda} (\xi_{\ell_1, i_1}^{T,p} + \xi_{\ell_1, i_1}^{R,q}(t)))} \times e^{j\frac{2\pi}{\lambda} v_R t \cos(\alpha_{\ell_1, i_1}^R(t) - \gamma_R) \cos \beta_{\ell_1, i_1}^R(t)} e^{-j2\pi f \tau_{\ell_1}^{\text{SB}}(t)}, \quad (23)$$

$$H_{pq}^{\text{DB-NLoS}}(t, f) = \sqrt{\frac{\eta_{\text{DB}}}{K_{\text{Rice}}^{\text{vir}} + 1}} \times \sum_{\ell_2=1}^{L_2} \sum_{i_2=1}^{I_2} \sqrt{\frac{P_{\ell_2}}{I_2}} \sum_{m=1}^M \sum_{n=1}^N \frac{1}{\sqrt{MN}} \chi_{mn}(t) e^{j\varphi_{mn}(t)} \times e^{j(\varphi_{\ell_2, i_2} - \frac{2\pi}{\lambda} (\xi_{\ell_2, i_2}^{T,p} + \xi_{\ell_2, i_2}^{R,q} + \xi_{\ell_2, mn}^{R,q}(t)))} \times e^{j\frac{2\pi}{\lambda} v_R t \cos(\alpha_{\ell_2, mn}^R(t) - \gamma_R) \cos \beta_{\ell_2, mn}^R(t)} e^{-j2\pi f \tau_{\ell_2}^{\text{DB}}(t)}.$$

Then, by dividing the components through RIS ($H_{pq}^{\text{V-LoS}}(t, f)$ and $H_{pq}^{\text{DB-NLoS}}(t, f)$) into three sub-components, that is, the propagation from Tx to RIS, the reflection of RIS, and the propagation from RIS to MR, respectively, $H_{pq}(t, f)$ can be re-expressed as (25), shown at the bottom of the page, where $\mathbf{h}_{\text{RIS}}^p(t, f) \in \mathbb{C}^{M \times 1}$ is the channel vector from p -th transmitting antenna to the RIS, $\mathbf{h}_q^{\text{RIS}}(t, f) \in \mathbb{C}^{1 \times MN}$ represents the channel vector from RIS to the q -th receiving antenna, and $\Phi_{\text{RIS}}(t) = \text{diag}\{\chi_{11}(t)e^{j\varphi_{11}(t)}, \dots, \chi_{mn}(t)e^{j\varphi_{mn}(t)}, \dots, \chi_{MN}(t)e^{j\varphi_{MN}(t)}\} \in \mathbb{C}^{MN \times MN}$ is a diagonal matrix standing for the reflection coefficients of the RIS units. Therefore, the overall cascaded channel frequency response matrix between Tx and MR, denoted by $\mathbf{H}(t, f) = [H_{pq}(t, f)]_{M_R \times M_T}$, can be re-expressed as

$$\mathbf{H}(t, f) = \underbrace{\mathbf{H}^{\text{SB-NLoS}}(t, f)}_{\text{no-RIS}} + \underbrace{\mathbf{H}_{\text{MR}}^{\text{RIS}}(t, f) \times \Phi_{\text{RIS}}(t) \times \mathbf{H}_{\text{RIS}}^{\text{Tx}}(t, f)}_{\text{RIS-assisted}}, \quad (26)$$

where $\mathbf{H}^{\text{SB-NLoS}}(t, f) = [H_{pq}^{\text{SB-NLoS}}(t, f)]_{M_R \times M_T}$ is the channel frequency response matrix that is independent of RIS, which can be used to characterize the multipath Rayleigh fading channels between the Tx and MR in conventional no-RIS communication systems, $\mathbf{H}_{\text{RIS}}^{\text{Tx}}(t, f) = [\mathbf{h}_{\text{RIS}}^{p=1}(t, f), \mathbf{h}_{\text{RIS}}^{p=2}(t, f), \dots, \mathbf{h}_{\text{RIS}}^{p=M_T}(t, f)] \in \mathbb{C}^{MN \times M_T}$ denotes the channel frequency response matrix between the Tx and RIS, and $\mathbf{H}_{\text{MR}}^{\text{RIS}}(t, f) =$

$$H_{pq}(t, f) = H_{pq}^{\text{SB-NLoS}}(t, f) + \underbrace{\begin{bmatrix} e^{-j\frac{2\pi}{\lambda} (\xi_{11}^{R,q}(t) - v_R t \cos(\alpha_{11}^R(t) - \gamma_R) \cos \beta_{11}^R(t))} e^{-j2\pi f \xi_{\text{RIS}}^R(t)/c} \\ \vdots \\ e^{-j\frac{2\pi}{\lambda} (\xi_{mn}^{R,q}(t) - v_R t \cos(\alpha_{mn}^R(t) - \gamma_R) \cos \beta_{mn}^R(t))} e^{-j2\pi f \xi_{\text{RIS}}^R(t)/c} \\ \vdots \\ e^{-j\frac{2\pi}{\lambda} (\xi_{MN}^{R,q}(t) - v_R t \cos(\alpha_{MN}^R(t) - \gamma_R) \cos \beta_{MN}^R(t))} e^{-j2\pi f \xi_{\text{RIS}}^R(t)/c} \end{bmatrix}^T}_{\mathbf{h}_q^{\text{RIS}}(t, f)} \times \underbrace{\begin{bmatrix} \sqrt{\frac{K_{\text{Rice}}^{\text{vir}}}{K_{\text{Rice}}^{\text{vir}} + 1}} e^{-j\frac{2\pi}{\lambda} \xi_{11}^{T,p}} e^{-j2\pi f \xi_{\text{RIS}}^T/c} \\ + \sqrt{\frac{\eta_{\text{DB}}}{K_{\text{Rice}}^{\text{vir}} + 1}} \sum_{\ell_2=1}^{L_2} \sum_{i_2=1}^{I_2} \sqrt{\frac{P_{\ell_2}}{I_2}} e^{j(\varphi_{\ell_2, i_2} - \frac{2\pi}{\lambda} (\xi_{\ell_2, i_2}^{T,p} + \xi_{\ell_2, i_2}^{R,q} + \xi_{\ell_2, 11}^{R,q}(t)))} e^{-j2\pi f (\xi_{\ell_2}^T + \xi_{\text{RIS}}^{\ell_2})/c} \\ \vdots \\ \sqrt{\frac{K_{\text{Rice}}^{\text{vir}}}{K_{\text{Rice}}^{\text{vir}} + 1}} e^{-j\frac{2\pi}{\lambda} \xi_{mn}^{T,p}} e^{-j2\pi f \xi_{\text{RIS}}^T/c} \\ + \sqrt{\frac{\eta_{\text{DB}}}{K_{\text{Rice}}^{\text{vir}} + 1}} \sum_{\ell_2=1}^{L_2} \sum_{i_2=1}^{I_2} \sqrt{\frac{P_{\ell_2}}{I_2}} e^{j(\varphi_{\ell_2, i_2} - \frac{2\pi}{\lambda} (\xi_{\ell_2, i_2}^{T,p} + \xi_{\ell_2, i_2}^{R,q} + \xi_{\ell_2, mn}^{R,q}(t)))} e^{-j2\pi f (\xi_{\ell_2}^T + \xi_{\text{RIS}}^{\ell_2})/c} \\ \vdots \\ \sqrt{\frac{K_{\text{Rice}}^{\text{vir}}}{K_{\text{Rice}}^{\text{vir}} + 1}} e^{-j\frac{2\pi}{\lambda} \xi_{MN}^{T,p}} e^{-j2\pi f \xi_{\text{RIS}}^T/c} \\ + \sqrt{\frac{\eta_{\text{DB}}}{K_{\text{Rice}}^{\text{vir}} + 1}} \sum_{\ell_2=1}^{L_2} \sum_{i_2=1}^{I_2} \sqrt{\frac{P_{\ell_2}}{I_2}} e^{j(\varphi_{\ell_2, i_2} - \frac{2\pi}{\lambda} (\xi_{\ell_2, i_2}^{T,p} + \xi_{\ell_2, i_2}^{R,q} + \xi_{\ell_2, MN}^{R,q}(t)))} e^{-j2\pi f (\xi_{\ell_2}^T + \xi_{\text{RIS}}^{\ell_2})/c} \end{bmatrix}}_{\mathbf{h}_{\text{RIS}}^p(t, f)} \times \Phi_{\text{RIS}}(t) \times \quad (25)$$

$[\mathbf{h}_{q=1}^{\text{RIS}}(t, f); \mathbf{h}_{q=2}^{\text{RIS}}(t, f); \dots; \mathbf{h}_{q=M_R}^{\text{RIS}}(t, f)] \in \mathbb{C}^{M_R \times MN}$ stands for the channel frequency response matrix between the RIS and MR. It is worth mentioning that the proposed model in frequency domain, that is, $\mathbf{H}(t, f)$, has a similar form as those in [9] and [23], however, the models in [9] and [23] are not appropriate for describing the realistic propagation environments and are mainly for narrowband stationary channels, which, as a consequence, will result in an inaccurate system performance evaluation of the RIS-assisted communications. By substituting the model parameters derived in sub-section II.B, they are, the distances, angles, and delays, into (4)-(7) and (22)-(26), respectively, the channel matrix of the proposed channel model in time- and frequency-domain can be obtained, which can be further used to describe various RIS-assisted wireless communication channels. For example, by only considering the V-LoS component, the proposed channel model can be used to describe the condition in which the network operates in a LoS setting; by only considering the SB-NLoS component, the model can be used to depict the conventional Rayleigh channels without RIS. Nevertheless, the phase response of the RIS units should be carefully designed to realize the manipulated waves being reflected toward the MR.

Many algorithms have been proposed to optimize the RIS reflection phases [8]–[12]; however, they are mainly based on simplistic channel models and cannot be extended for further analysis. Though generalized law of reflection has been applied in [18], [21], [23], and [26] to derive the phase shift models, they were based on simplified virtual environment and ignored the practical deployment of RIS, thus are not appropriate for effectively characterizing the reflection phases of RIS units. Considering that the signal power of the LoS component is generally much stronger than that of the scattered components, in the following we present a sub-optimal solution with low complexity to derive the analytical expression of the reflecting phases of the RIS units by optimizing the V-LoS link only. The basic idea is to optimize the reflecting phases of different RIS units so as to compensate the phase differences caused by the location of the units, as a consequence the reflecting waves from different units are combined constructively at the MR [28]. For clarify, we visualize the Tx and MR as a point, this can be achieved by performing transmit beamforming at the Tx and receive beamforming at the MR to offset the phase differences introduced by different antennas, respectively. From sub-section II.B-1) we know that the distances from the centers of Tx and MR arrays to the (m, n) -th RIS unit can be expressed as $\xi_{mn}^T = \|\mathbf{d}_{\text{RIS}}^{\text{MT}} + \mathbf{A}_{mn}^{\text{RIS}}\|$ and $\xi_{mn}^R(t) = \|\mathbf{d}_{\text{RIS}}^{\text{MR}}(0) + \mathbf{A}_{mn}^{\text{RIS}} - \Delta \mathbf{d}_{\text{MR}}(t)\|$, respectively. It is worth mentioning that the Taylor series expansions of $(1+\zeta)^{1/2}$ at ζ_0 can be expressed as $(1+\zeta)^{1/2} = (1+\zeta_0)^{1/2} + \frac{1}{2\sqrt{1+\zeta_0}}(\zeta - \zeta_0) + \mathcal{O}(\zeta - \zeta_0)$. Then, by imposing $\zeta_0 = 0$ and ignoring the negligible higher-order terms, distances ξ_{mn}^T and $\xi_{mn}^R(t)$ can be respectively approximated by

$$\begin{aligned} \xi_{mn}^T &\approx \xi_{\text{RIS}}^T + \frac{z_I - H_0}{\xi_{\text{RIS}}^T} k_n d_N \cos \epsilon_I \\ &+ \frac{y_I}{\xi_{\text{RIS}}^T} (k_m d_M \sin \theta_I - k_n d_N \cos \theta_I \sin \epsilon_I) \end{aligned}$$

$$+ \frac{x_I}{\xi_{\text{RIS}}^T} (k_m d_M \cos \theta_I + k_n d_N \sin \theta_I \sin \epsilon_I), \quad (27)$$

$$\begin{aligned} \xi_{mn}^R(t) &\approx \xi_{\text{RIS}}^R(t) + \frac{z_I}{\xi_{\text{RIS}}^R(t)} k_n d_N \cos \epsilon_I \\ &+ \frac{x_I - \xi_R - v_R t \cos \gamma_R}{\xi_{\text{RIS}}^R(t)} \\ &\times (k_m d_M \cos \theta_I + k_n d_N \sin \theta_I \sin \epsilon_I) \\ &+ \frac{y_I - v_R t \sin \gamma_R}{\xi_{\text{RIS}}^R(t)} \\ &\times (k_m d_M \sin \theta_I - k_n d_N \cos \theta_I \sin \epsilon_I). \quad (28) \end{aligned}$$

Therefore, the distance-related phase shift of the ray via the (m, n) -th unit can be expressed as $-\frac{2\pi}{\lambda}(\xi_{mn}^T + \xi_{mn}^R(t))$. Then, the RIS controller will provide a phase shift of $\varphi_{mn}(t)$ to compensate the phase difference of different rays so that the received waves are combined constructively, that is, $\varphi_{mn}(t) - \frac{2\pi}{\lambda}(\xi_{mn}^T + \xi_{mn}^R(t)) = \Phi$, where Φ is a constant value. We denote $\varphi_0^{\text{RIS}}(t)$ by the phase shift at the center of the RIS, thus $\varphi_0^{\text{RIS}}(t) - \frac{2\pi}{\lambda}(\xi_{\text{RIS}}^T + \xi_{\text{RIS}}^R(t)) = \Phi$. Therefore, the reflecting phase of the RIS unit can be expressed as

$$\begin{aligned} \varphi_{mn}(t) &= \varphi_0^{\text{RIS}}(t) + \frac{2\pi}{\lambda} \times \left(\left(\frac{x_I}{\xi_{\text{RIS}}^T} + \frac{x_I - \xi_R - v_R t \cos \gamma_R}{\xi_{\text{RIS}}^R(t)} \right) \right. \\ &\times (k_m d_M \cos \theta_I + k_n d_N \sin \theta_I \sin \epsilon_I) \\ &+ \left(\frac{y_I}{\xi_{\text{RIS}}^T} + \frac{y_I - v_R t \sin \gamma_R}{\xi_{\text{RIS}}^R(t)} \right) \\ &\times (k_m d_M \sin \theta_I - k_n d_N \cos \theta_I \sin \epsilon_I) \\ &\left. + \left(\frac{z_I - H_0}{\xi_{\text{RIS}}^T} + \frac{z_I}{\xi_{\text{RIS}}^R(t)} \right) \times k_n d_N \cos \epsilon_I \right). \quad (29) \end{aligned}$$

It can be seen that the reflection phases of the RIS units are related to the locations of the Tx, RIS, and MR. Moreover, the reflection phases are time-variant due to the motion of the MR, which requires the time-varying program of the reflection phases. Note that the complex-exponential function $e^{j\Phi}$ is periodic with 2π and the phase shift provided by RIS units lies in the interval of $[0, 2\pi)$, thus the actual phase shift provided by the (m, n) -th RIS unit should be $\varphi_{mn}(t) \bmod 2\pi$.

III. STATISTICAL PROPERTIES OF THE PROPOSED RIS CHANNEL MODEL

In this section, we investigate the channel statistical properties, including the spatial-temporal (ST) CCFs and temporal ACFs, of the proposed non-stationary 3D MIMO RIS channel model.

A. The ST CCFs

The normalized spatial-temporal cross-correlation functions of the proposed channel model can be defined as the correlations between two different channel coefficients $h_{pq}(t)$ and $h_{p'q'}(t)$, where $p' = 1, 2, \dots, M_T$ and $q' = 1, 2, \dots, M_R$, being expressed as [41]

$$\begin{aligned} \rho_{(p,q),(p',q')}(t; \Delta p, \Delta q, \Delta t) &= \frac{\mathbb{E}[h_{pq}^*(t) h_{p'q'}(t + \Delta t)]}{\sqrt{\mathbb{E}[\|h_{pq}(t)\|^2] \mathbb{E}[\|h_{p'q'}(t + \Delta t)\|^2]}}, \quad (30) \end{aligned}$$

where Δt denotes the time difference, $\mathbb{E}[\cdot]$ is the statistical average, the superscript $[\cdot]^*$ is the complex conjugation operator, $\Delta p = |p' - p|\delta_T/\lambda$ is the normalized transmit antenna spacing between the p -th and p' -th antenna, and $\Delta q = |q' - q|\delta_R/\lambda$ is the normalized receive antenna spacing between the q -th and q' -th antenna. In addition, $h_{pq}(t)$ and $h_{p'q'}(t)$ denote the complex channel coefficients of the $(p \rightarrow q)$ -th and $(p' \rightarrow q')$ -th transmit-receive antenna pair, respectively.

It is generally assumed that the V-LoS, SB-NLoS, and DB-NLoS components are independent with each other [40]. Then, by imposing $\Delta t = 0$ and substituting (5) into (30), we get the spatial CCF of the V-LoS component $\rho_{(p,q),(p',q')}^{\text{V-LoS}}(t; \Delta p, \Delta q)$, which can be expressed as

$$\begin{aligned} & \rho_{(p,q),(p',q')}^{\text{V-LoS}}(t; \Delta p, \Delta q) \\ &= \frac{1}{MN} \sum_{m=1}^M \sum_{n=1}^N e^{j \frac{2\pi}{\lambda} (\xi_{mn}^{T,p} - \xi_{mn}^{T,p'} + \xi_{mn}^{R,q}(t) - \xi_{mn}^{R,q'}(t))}. \end{aligned} \quad (31)$$

By imposing $\Delta t = 0$ and substituting (6) into (30), the spatial CCFs of the SB-NLoS components $\rho_{(p,q),(p',q')}^{\text{SB-NLoS}}(t; \Delta p, \Delta q)$ via the reflection of cluster S_{ℓ_1} in cluster set C^{L_1} can be expressed as

$$\begin{aligned} & \rho_{(p,q),(p',q'),\ell_1}^{\text{SB-NLoS}}(t; \Delta p, \Delta q) \\ &= \int_{-\pi}^{\pi} \int_{-\pi}^{\pi} e^{j \frac{2\pi}{\lambda} (\xi_{\ell_1}^{T,p} - \xi_{\ell_1}^{T,p'} + \xi_{\ell_1}^{R,q}(t) - \xi_{\ell_1}^{R,q'}(t))} \\ & \quad \times f(\alpha_{\ell_1}^T, \beta_{\ell_1}^T) d(\alpha_{\ell_1}^T, \beta_{\ell_1}^T), \end{aligned} \quad (32)$$

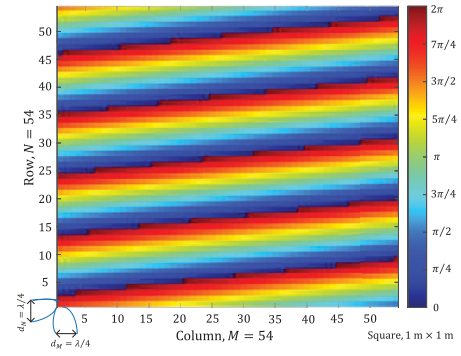
where $f(\alpha_{\ell_1}^T, \beta_{\ell_1}^T)$ denotes the joint probability density function (PDF) of the azimuth angle $\alpha_{\ell_1}^T$ and elevation angle $\beta_{\ell_1}^T$ of cluster S_{ℓ_1} . Furthermore, the spatial CCFs of the DB-NLoS components $\rho_{(p,q),(p',q')}^{\text{DB-NLoS}}(t; \Delta p, \Delta q)$ via the reflection of cluster S_{ℓ_2} and RIS can be obtained by imposing $\Delta t = 0$ and substituting (7) into (30), which is expressed as

$$\begin{aligned} & \rho_{(p,q),(p',q'),\ell_2}^{\text{DB-NLoS}}(t; \Delta p, \Delta q) = \frac{1}{MN} \\ & \times \int_{-\pi}^{\pi} \int_{-\pi}^{\pi} \left(\sum_{m=1}^M \sum_{n=1}^N e^{j \frac{2\pi}{\lambda} (\xi_{\ell_2}^{T,p} - \xi_{\ell_2}^{T,p'} + \xi_{\ell_2,mn}^{R,q}(t) - \xi_{\ell_2,mn}^{R,q'}(t))} \right) \\ & \times f(\alpha_{\ell_2}^T, \beta_{\ell_2}^T) d(\alpha_{\ell_2}^T, \beta_{\ell_2}^T), \end{aligned} \quad (33)$$

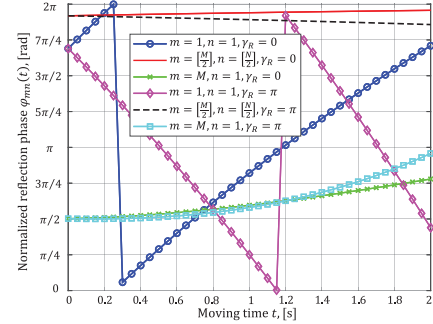
where $f(\alpha_{\ell_2}^T, \beta_{\ell_2}^T)$ is the joint PDF of the azimuth angle $\alpha_{\ell_2}^T$ and elevation angle $\beta_{\ell_2}^T$ of the cluster S_{ℓ_2} . It should be noted that in cluster-based channel model, one cluster corresponds to one distinguishable propagation path comprising of many unresolvable rays, and hence the values of the signal directions are limited to a certain range. Here we adopt the truncated Gaussian PDF to characterize the angular distribution [42], hence the PDF for the waves with direction θ being limited within the interval from θ_{low} to θ_{up} , i.e., $\theta \in [\theta_{\text{low}}, \theta_{\text{up}}]$, can be expressed as

$$f(\theta, \mu_{\theta}, \sigma_{\theta}, \theta_{\text{low}}, \theta_{\text{up}}) = \frac{\frac{1}{\sigma_{\theta}} \phi\left(\frac{\theta - \mu_{\theta}}{\sigma_{\theta}}\right)}{\Phi\left(\frac{\theta_{\text{up}} - \mu_{\theta}}{\sigma_{\theta}}\right) - \Phi\left(\frac{\theta_{\text{low}} - \mu_{\theta}}{\sigma_{\theta}}\right)}, \quad (34)$$

where μ_{θ} and σ_{θ} denote the mean value and angle spread of the signal direction θ , respectively; θ_{low} and θ_{up} are the lower and upper bounds of the truncated Gaussian distributed signal direction θ , respectively. Moreover, $\phi(\epsilon)$ denotes the



(a) Normalized reflection phases over the RIS array



(b) Normalized time-varying reflection phases

Fig. 4. Normalized reflection phases of the RIS units. (a) Stationary scenario, $v_R = 0$; (b) Non-stationary scenario.

PDF of the standard normal distributed random variable ϵ , which can be expressed as $\phi(\epsilon) = \frac{1}{\sqrt{2\pi}} \exp\{-\frac{\epsilon^2}{2}\}$; while $\Phi(\epsilon) = \int_{-\infty}^{\epsilon} \phi(\epsilon') d\epsilon' = \frac{1}{2} (1 + \text{erf}(\frac{\epsilon}{\sqrt{2}}))$ represents the cumulative distribution function (CDF) of the standard normal distributed random variable ϵ , where $\text{erf}(\cdot)$ is the Gauss error function. Since the azimuth and elevation angles are generally modeled as being independent of each other, the joint PDFs in (32) and (33) can be derived from (34) as $f(\alpha^T, \beta^T) = f(\alpha^T, \mu_{\alpha^T}, \sigma_{\alpha^T}, \alpha_{\text{low}}^T, \alpha_{\text{up}}^T) f(\beta^T, \mu_{\beta^T}, \sigma_{\beta^T}, \beta_{\text{low}}^T, \beta_{\text{up}}^T)$.

B. The Temporal ACFs

The temporal ACF of the proposed channel model can be obtained by imposing $p' = p$ and $q' = q$ in (30), which is expressed as

$$\rho_{(p,q)}(t, \Delta t) = \frac{\mathbb{E}[h_{pq}^*(t) h_{pq}(t + \Delta t)]}{\sqrt{\mathbb{E}[|h_{pq}(t)|^2] \mathbb{E}[|h_{pq}(t + \Delta t)|^2]}}. \quad (35)$$

Then, by substituting (5) into (35), the ACF of the V-LoS component can be expressed as

$$\begin{aligned} & \rho_{(p,q)}^{\text{V-LoS}}(t, \Delta t) \\ &= \frac{1}{MN} \sum_{m=1}^M \sum_{n=1}^N e^{j \frac{2\pi}{\lambda} (\xi_{mn}^{R,q}(t) - \xi_{mn}^{R,q}(t + \Delta t))} \\ & \times e^{j \frac{2\pi}{\lambda} (v_R \cdot (t + \Delta t) \cos(\alpha_{mn}^R(t + \Delta t) - \gamma_R) \cos \beta_{mn}^R(t + \Delta t))} \\ & \times e^{-j \frac{2\pi}{\lambda} v_R t \cos(\alpha_{mn}^R(t) - \gamma_R) \cos \beta_{mn}^R(t)}. \end{aligned} \quad (36)$$

By substituting (4) into (35), we can derive the ACF of the SB-NLoS components via the reflection of cluster S_{ℓ_1} , which

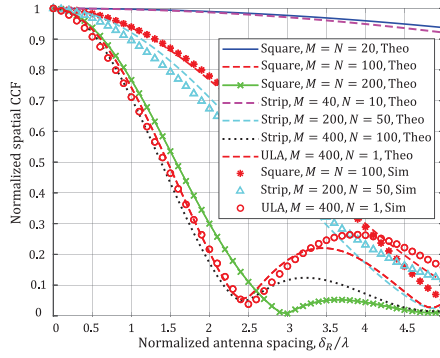


Fig. 5. Spatial CCF of the proposed channel model for the V-LoS component under different RIS configurations and RIS unit numbers when $t = 1$ s, where “Theo” means theoretical results and “Sim” means simulated results.

can be expressed as

$$\begin{aligned} \rho_{(p,q),\ell_1}^{\text{SB-NLoS}}(t, \Delta t) &= \int_{-\pi}^{\pi} \int_{-\pi}^{\pi} e^{j \frac{2\pi}{\lambda} (\xi_{\ell_1, q}^{R, q}(t) - \xi_{\ell_1, q}^{R, q}(t + \Delta t))} \\ &\quad \times e^{j \frac{2\pi}{\lambda} (v_R \cdot (t + \Delta t) \cos(\alpha_{\ell_1, i_1}^R(t + \Delta t) - \gamma_R) \cos \beta_{\ell_1, i_1}^R(t + \Delta t))} \\ &\quad \times e^{-j \frac{2\pi}{\lambda} v_R t \cos(\alpha_{\ell_1, i_1}^R(t) - \gamma_R) \cos \beta_{\ell_1, i_1}^R(t)} \\ &\quad \times f(\alpha_{\ell_1}^T, \beta_{\ell_1}^T) d(\alpha_{\ell_1}^T, \beta_{\ell_1}^T). \end{aligned} \quad (37)$$

Finally, the ACF of the DB-NLoS components via the reflection of cluster S_{ℓ_2} and RIS can be obtained by substituting (7) into (35), which is expressed as

$$\begin{aligned} \rho_{(p,q),\ell_2}^{\text{DB-NLoS}}(t, \Delta t) &= \int_{-\pi}^{\pi} \int_{-\pi}^{\pi} \sum_{m=1}^M \sum_{n=1}^N \frac{e^{j \frac{2\pi}{\lambda} (\xi_{\ell_2, mn}^{R, q}(t) - \xi_{\ell_2, mn}^{R, q}(t + \Delta t))}}{MN} \\ &\quad \times e^{j \frac{2\pi}{\lambda} (v_R \cdot (t + \Delta t) \cos(\alpha_{\ell_2, mn}^R(t + \Delta t) - \gamma_R) \cos \beta_{\ell_2, mn}^R(t + \Delta t))} \\ &\quad \times e^{-j \frac{2\pi}{\lambda} v_R t \cos(\alpha_{mn}^R(t) - \gamma_R) \cos \beta_{mn}^R(t)} \\ &\quad \times f(\alpha_{\ell_2}^T, \beta_{\ell_2}^T) d(\alpha_{\ell_2}^T, \beta_{\ell_2}^T). \end{aligned} \quad (38)$$

It can be seen that the temporal ACFs of the proposed channel model dependent not only on the time difference Δt , but also on the absolute time t , which meets with the results for non-stationary channel models.

IV. RESULTS AND DISCUSSIONS

In this section, we mainly investigate the channel propagation characteristics of the RIS-assisted components via simulations, the study of the propagation that is independent of RIS can refer to our previous work in [30], [35], and [41].

A. Simulation Setup

The proposed RIS channel model is operated at a carrier frequency of $f_c = 4$ GHz. The model parameters used in the simulations are listed here or specified otherwise: $M_T = 4$, $M_R = 6$, $\xi_R = 100$ m, $H_0 = 25$ m, $\delta_T = \delta_R = \lambda/2$, $\psi_T = \pi/3$, $\phi_T = \pi/4$, $\psi_R = \pi/4$, $\phi_R = \pi/4$. For cluster

S_{ℓ_1} in cluster set C^{L_1} , we set $\xi_{\ell_1}^T = 80$ m, $\mu_{\alpha_{\ell_1}^T} = 1.047$ rad, $\sigma_{\alpha_{\ell_1}^T} = 0.524$ rad, $\mu_{\beta_{\ell_1}^T} = -0.26$ rad, and $\sigma_{\beta_{\ell_1}^T} = 0.11$ rad, and for cluster S_{ℓ_2} in cluster set C^{L_2} , we set $\xi_{\ell_2}^T = 65$ m, $\mu_{\alpha_{\ell_2}^T} = 1.396$ rad, $\sigma_{\alpha_{\ell_2}^T} = 0.54$ rad, $\mu_{\beta_{\ell_2}^T} = 0.405$ rad, and $\sigma_{\beta_{\ell_2}^T} = 0.105$ rad, respectively [42]. The RIS is located at $(x_I, y_I, z_I) = (75 \text{ m}, 20 \text{ m}, 15 \text{ m})$ with the rotation angles $\theta_I = -20^\circ$ and $\epsilon_I = -5^\circ$, and the size of the RIS unit is set as $d_M = d_N = \lambda/4$. Two kinds of configurations of RIS with $MN = 10^4$ are considered, that is, RIS_A with strip configuration $M = 200, N = 50$ and RIS_B with square configuration $M = N = 100$, respectively. Finally, the moving speed and direction of the MR are set as $v_R = 5$ m/s and $\gamma_R = 0$, respectively.

B. Performance Analysis

1) *Phase Response of the RIS*: Based on (29), the normalized RIS reflection phase in a $1 \text{ m} \times 1 \text{ m}$ square RIS array is shown in Fig. 4, where the reflection phase is normalized with respect to 2π . Fig. 4(a) is the phase pattern of the overall RIS in a stationary scenario, that is, $v_R = 0$, whereas Fig. 4(b) shows the time-varying reflection phases of three representative units, i.e., two corner units ($m = 1, n = 1$ and $m = M, n = 1$) and one central unit ($m = \lceil \frac{M}{2} \rceil, n = \lceil \frac{N}{2} \rceil$). Fig. 4(a) indicates that the reflection phases of the RIS units show a periodicity of the phase values over the array, which means that different RIS units can have the same reflection phase in order to manipulate the incident waves towards the destination point. The RIS reflection phase pattern will change when the model parameters vary, however, the periodicity of the phase values of different RIS units still holds. The results in Fig. 4(b), on the other hand, reveal that the RIS reflection phase are time dependent due to the motion of the MR. Meanwhile, the RIS reflection phase show different time-varying properties when the MR adopts different mobility models. This arises for the necessity of time-varying control of RIS reflection phases. Nevertheless, (29) is sub-optimal without considering the multipath propagations from Tx to RIS and the wideband implementation of RIS, which is an urgent work to be solved in the future.

2) *Spatial CCFs*: By imposing $\Delta p = 0$ in (31), Fig. 5 shows the normalized spatial CCF of the proposed channel model for the V-LoS component with respect to the RIS unit numbers. It can be seen that the channel spatial CCF decreases as the antenna spacing increases, where the antenna spacing is normalized with respect to wavelength. Moreover, we observe that the channel spatial CCF shows more rapidly decline as the RIS unit number increases. This is mainly because that the RIS with more units has larger physical size, which causes larger spatial spread and more sparsely distributed power, resulting in smaller correlation [32]. The authors in [22] have demonstrated that the RIS configuration is an important factor in determining the performance of RIS. Therefore, in Fig. 5 we also study the impact of RIS configurations on channel spatial correlations by considering three different RIS configurations, they are, the square-, strip-, and ULA-configured RISs. The results show that the channel with square-configured RIS has largest spatial CCF, whereas the channel with ULA-configured

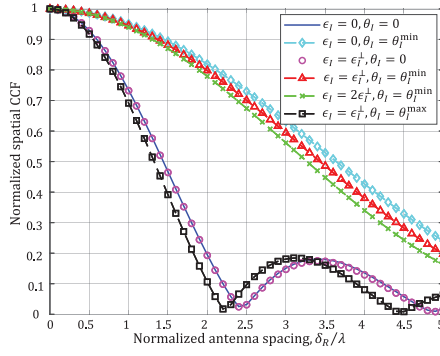


Fig. 6. Spatial CCF of the proposed channel model for the V-LoS component with RIS_A under different RIS orientation angles, where $(x_I, y_I, z_I) = (85 \text{ m}, 20 \text{ m}, 10 \text{ m})$, $\epsilon_I^\perp = -10.31^\circ$, $\theta_I^{\min} = -45^\circ$, and $\theta_I^{\max} = 14^\circ$.

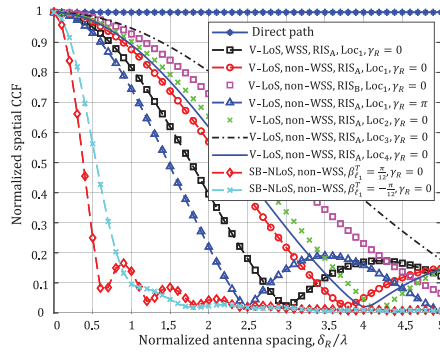


Fig. 7. Spatial CCF of the proposed channel model for different components and RIS locations, where $\text{Loc}_1 = (80 \text{ m}, 20 \text{ m}, 15 \text{ m})$, $\text{Loc}_2 = (80 \text{ m}, 20 \text{ m}, 35 \text{ m})$, $\text{Loc}_3 = (70 \text{ m}, 20 \text{ m}, 15 \text{ m})$, and $\text{Loc}_4 = (80 \text{ m}, 30 \text{ m}, 15 \text{ m})$.

RIS has smallest spatial CCF even with much few RIS units. In general, it requires a larger number of RIS units to compensate the very high pathloss; meanwhile, the ULA-configured RIS suffers from poor space efficiency especially when the unit number is large. In light of this, a strip-configured RIS is more realizable and helpful for the system to achieve higher data rate by spatial diversity as compared to the square- or ULA-configured RIS. Furthermore, the agreement between the theoretical and simulated results of the spatial CCFs under these three different RIS configurations verifies the correctness of the derived spatial CCF, which further implies that the RIS configuration is important in determining the communication performance.

Fig. 6 indicates that the spatial CCF of the proposed channel model has different values under different RIS orientation angles, which implies that it is important to take into account the RIS orientations in RIS-assisted channel modeling. Moreover, it shows that the channel shows smaller spatial CCFs when increasing the horizontal rotation angle from θ_I^{\min} to θ_I^{\max} , while the impact of vertical rotation angle ϵ_I is insignificant. Note that the RIS has the largest reflection aperture when it is deployed with rotation angle of ϵ_I^\perp and θ_I^{\min} , in this case the RIS delivers the most power from Tx to MR. In Fig. 7 we investigate the impact of RIS locations on channel spatial CCFs. We found that by increasing the distance between RIS and MR, the spatial CCFs increase. Moreover,

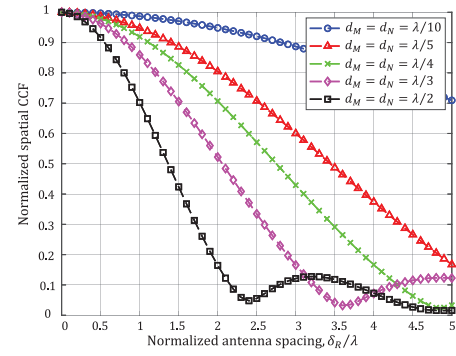


Fig. 8. Spatial CCF of the proposed channel model for the V-LoS component with RIS_A under different RIS unit sizes.

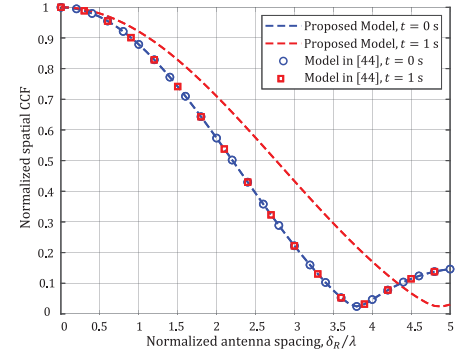


Fig. 9. Spatial CCF of the proposed channel model for the V-LoS component with RIS_A under different time instants.

we can see that different from the physical direct path with constant spatial CCFs, the V-LoS component can provide a NLoS-like decline on the spatial CCFs but the decline rate is more slighter than that of the actual cluster scattered SB-NLoS components. Meanwhile, Fig. 7 also reveals that the RIS configurations and moving direction of MR can affect the channel spatial CCFs, which is consistent with the results in Fig. 5.

In Fig. 8, we study the impact of RIS unit size of a strip-configured RIS, that is, RIS_A with $M = 200, N = 50$, on channel spatial CCF. The RIS unit size is typically among $\lambda/10 \sim \lambda/2$ [15], in Fig. 6 we set the RIS unit size as $\lambda/2 \times \lambda/2$, $\lambda/3 \times \lambda/3$, $\lambda/4 \times \lambda/4$, $\lambda/5 \times \lambda/5$, and $\lambda/10 \times \lambda/10$, respectively. It can be seen that as the unit size becomes larger, i.e., from $\lambda/10 \times \lambda/10$ to $\lambda/2 \times \lambda/2$, the spatial CCFs of the channel show a faster decline as the normalized antenna spacing increases. Although more RIS units can be integrated when RIS unit size is smaller, the channel with smaller RIS unit size shows higher spatial correlations, thus deteriorates the spatial diversity of the MIMO channel. The results from these typical parameter settings are enough to reveal the fact that by increasing the RIS unit size, the channel spatial CCF decreases, which indicates that a relatively larger RIS unit size will cause smaller channel spatial correlation, thus is more helpful for spatial diversity. In Fig. 9, we study the normalized spatial CCF of the proposed channel model under different time instants. It can be seen that the changing curves of the

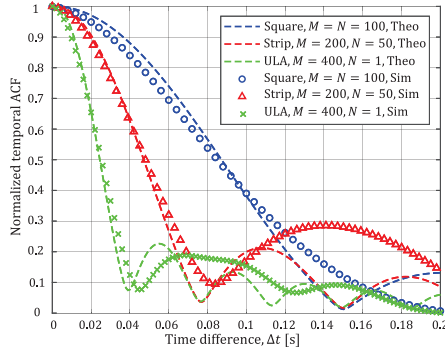


Fig. 10. Temporal ACF of the proposed channel model for the V-LoS component under different RIS configurations when $\gamma_R = \pi$ and $t = 2$ s, where “Theo” means theoretical results and “Sim” means simulated results.

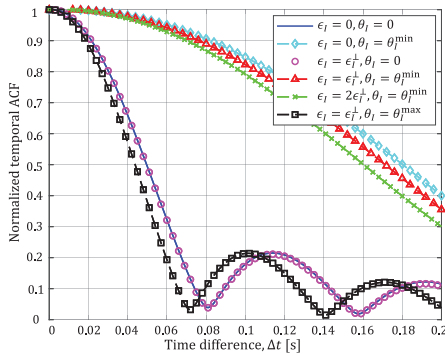


Fig. 11. Temporal ACF of the proposed channel model for the V-LoS component with RIS_A under different RIS orientation angles, where $(x_I, y_I, z_I) = (70 \text{ m}, 20 \text{ m}, 10 \text{ m})$, $\epsilon_I^\perp = -10.31^\circ$, $\theta_I^{\min} = -45^\circ$, and $\theta_I^{\max} = 14^\circ$.

spatial CCFs of the proposed channel model are in agreement with those of the channel model in [44] when $t = 0$ s, which verify the effectiveness of the proposed channel model. Moreover, we observe that the proposed channel model shows different spatial correlations under different time instants as in [43], whereas the channel model in [44] retains the same spatial correlation at different time instants. This can be interpreted by the fact that the proposed model in this paper is a non-stationary channel model, which shows different spatial correlations at different times; whereas the channel model in [44] is a stationary channel model, whose spatial correlation is independent of time. Overall, the proposed channel model is more useful to describe the realistic propagation environments, especially for the case when the user is in motion.

3) *Temporal ACFs*: The results in Fig. 10 show the theoretical and simulated results for the temporal ACFs of the proposed channel model under different RIS configurations. It can be seen that the theoretical curves fit the simulated curves well, which validate the accuracy of the derived temporal ACFs of the proposed channel model. Furthermore, the figure shows that different RIS configurations will cause different temporal correlations of the channel, which is in agreement with the results in Fig. 5. By comparing the results in Figs. 5 and 10, we conclude that the RIS configuration will affect the propagation characteristics of the channel, which is in agreement with the results in [22]. Generally, the channel with

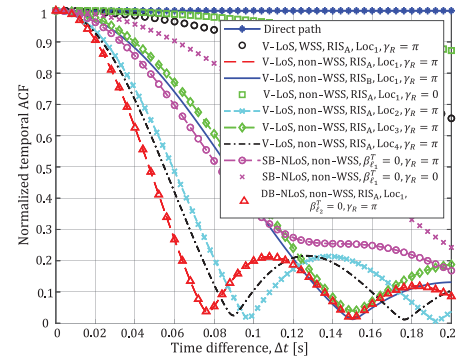


Fig. 12. Temporal ACF of the proposed channel model for different components and RIS locations, where $\text{Loc}_1 = (75 \text{ m}, 20 \text{ m}, 15 \text{ m})$, $\text{Loc}_2 = (75 \text{ m}, 20 \text{ m}, 35 \text{ m})$, $\text{Loc}_3 = (65 \text{ m}, 20 \text{ m}, 15 \text{ m})$, and $\text{Loc}_4 = (75 \text{ m}, 30 \text{ m}, 15 \text{ m})$.

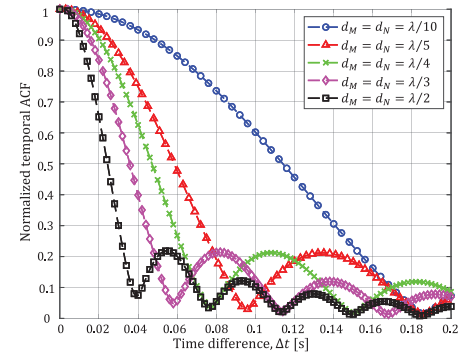


Fig. 13. Temporal ACF of the proposed channel model for the V-LoS component with RIS_A under different RIS unit sizes.

a strip-configured RIS can be more likely to realize higher data rate by spatial diversity and less frequently channel estimation by longer channel correlation time.

Then, in Fig. 11 the channel temporal ACFs with RIS_A under different RIS orientations are plotted. Similarly to the results in Fig. 6, the temporal ACFs show relatively faster decline when the horizontal rotation angle increases from θ_I^{\min} to θ_I^{\max} , and when the vertical rotation angle decreases from 0 to $2\epsilon_I^\perp$. When the RIS orientation is set as $\epsilon_I = \epsilon_I^\perp$ and $\theta_I = \theta_I^{\min}$, it has the largest reflection aperture and causes relatively longer channel correlation time but relatively higher link spatial correlation. Therefore, the orientation of RIS should be properly designed to balance the reflection aperture of RIS, channel correlation time, and link spatial correlation. The temporal ACFs of the proposed channel model under different RIS locations is plotted in Fig. 12. Similarly to the spatial CCFs in Fig. 7, the increasing of the distance between RIS and MR will cause slower decline of the temporal ACFs and longer channel correlation time, thus channel estimation can be performed less frequently and more saved time can be used for data transmission. Apart from the similar findings as described in Fig. 7, Fig. 12 implies that the curve of the temporal ACF for the DB-NLoS component coincides with that of the V-LoS component, this is in consistent with the results in [40] that the propagation of the first-bounce and that of the last-bounce are independent in double-bounced links.

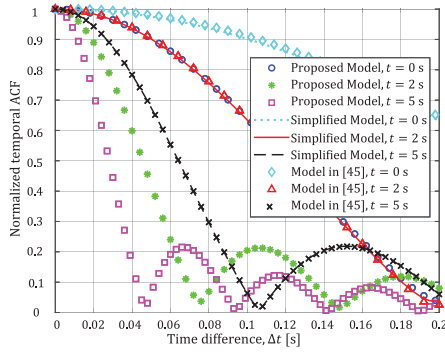


Fig. 14. Temporal ACF of the proposed channel model for the V-LoS component with RIS_A under different time instants.

By substituting (5) into (35), the temporal ACFs of the V-LoS component with RIS_A under different RIS unit sizes are illustrated in Fig. 13. It shows that the RIS with a larger unit size can result in faster decline of the temporal ACFs as compared to the RIS with a relatively smaller unit size. Therefore, a smaller RIS unit size is helpful to ensure a longer channel coherence time, thus less frequently estimation of the channel, which means more saved time can be used for information transmission. By comparing the results in Figs. 8 and 13, we find that the RIS unit size has different impacts on the channel spatial correlation and temporal correlation. Consequently, this indicates that the design of the RIS unit size in practical RIS-assisted communication systems should be well balanced according to the specific communication requirements, neither larger or smaller is better. Fig. 14 shows the normalized temporal ACF of the proposed channel model and that of the channel model in [45] under different time instants, where the “Simplified Model” is derived from the proposed channel model by ignoring the Doppler frequency. It is worthy to note that the channel model in [45] is restricted for single-antenna systems, thus we set $M_T = 1$ and $M_R = 1$ for the proposed channel model to derive Fig. 14. It shows that the temporal ACF decreases as the time difference Δt increases and the temporal ACF has different values at different time instants, which means that the temporal ACF of the proposed channel model is dependent on the moving time as in [26], thus validates the non-stationary property of the proposed channel model. Furthermore, we find that the temporal ACFs of the proposed channel model are different from those of the channel model in [45], whereas the temporal ACFs of the simplified model match well with those of the channel model in [45]. This is in consistent with the fact that the channel model in [45] does not consider the Doppler frequency, thus the results of the simplified model will nicely match with those from the channel model in [45]. This also verifies the accuracy of the proposed channel model and highlights its advantage to describe non-stationary channels.

V. CONCLUSION

In this paper, we have developed a general end-to-end 3D wideband non-stationary MIMO GBSM for characterizing the multipath small-scale fading of the RIS-assisted wireless communication channels. By modeling the RIS as a virtual cluster, the complex CIR of the proposed channel model

has been generalized and modeled by the proposed formulas. The equivalence between end-to-end and cascaded modeling of RIS channels has been verified and a sub-optimal solution with low complexity is used to derive the time-varying RIS reflection phases. The proposed modeling solution can provide a general and accurate description of the physical propagation characteristics of realistic RIS-assisted wireless communication channels, which can be helpful for researchers in algorithm validations, system designs, and performance analyses via simulations. The results show that the physical properties of RIS including unit numbers, unit sizes, array configurations, and array orientations can have a great impact on channel statistical properties. Generally, a strip-configured RIS is preferred as compared to square/ULA-configured RIS, while the design of unit numbers, unit sizes, and array orientations should be balanced according to performance requirements such as channel coherence time and received power.

As future work, we can point out five potential directions: i) develop efficient algorithms to simplify the model for more insightful results with the consideration of ensuring the model accuracy; ii) wideband realization of RIS; iii) develop efficient algorithms to derive the optimal reflection phases; iv) conduct measurements to further validate the proposed model; v) evaluate the SNR performance at the receiver under different RIS configurations.

REFERENCES

- [1] F. Boccardi, R. W. Heath, Jr., A. Lozano, T. L. Marzetta, and P. Popovski, “Five disruptive technology directions for 5G,” *IEEE Commun. Mag.*, vol. 52, no. 2, pp. 74–80, Feb. 2014.
- [2] W. Saad, M. Bennis, and M. Chen, “A vision of 6G wireless systems: Applications, trends, technologies, and open research problems,” *IEEE Netw.*, vol. 34, no. 3, pp. 134–142, May/Jun. 2020.
- [3] Q. Wu and R. Zhang, “Towards smart and reconfigurable environment: Intelligent reflecting surface aided wireless network,” *IEEE Commun. Mag.*, vol. 58, no. 1, pp. 106–112, Jan. 2020.
- [4] M. D. Renzo *et al.*, “Smart radio environments empowered by reconfigurable AI meta-surfaces: An idea whose time has come,” *EURASIP J. Wireless Commun. Netw.*, vol. 2019, no. 1, pp. 1–20, May 2019.
- [5] E. Basar, M. Di Renzo, J. De Rosny, M. Debbah, M. Alouini, and R. Zhang, “Wireless communications through reconfigurable intelligent surfaces,” *IEEE Access*, vol. 7, pp. 116753–116773, 2019.
- [6] J. Huang and J. A. Encinar, *Reflectarray Antennas*. Hoboken, NJ, USA: Wiley, 2008.
- [7] C. Liaskos, S. Nie, A. Tsioliaridou, A. Pitsillides, S. Ioannidis, and I. Akyildiz, “A new wireless communication paradigm through software-controlled metasurfaces,” *IEEE Commun. Mag.*, vol. 56, no. 9, pp. 162–169, Sep. 2018.
- [8] C. Huang, A. Zappone, G. C. Alexandropoulos, M. Debbah, and C. Yuen, “Reconfigurable intelligent surfaces for energy efficiency in wireless communication,” *IEEE Trans. Wireless Commun.*, vol. 18, no. 8, pp. 4157–4170, Aug. 2019.
- [9] Q. Wu and R. Zhang, “Intelligent reflecting surface enhanced wireless network via joint active and passive beamforming,” *IEEE Trans. Wireless Commun.*, vol. 18, no. 11, pp. 5394–5409, Nov. 2019.
- [10] Y. Pan, K. Wang, C. Pan, H. Zhu, and J. Wang, “UAV-assisted and intelligent reflecting surfaces-supported terahertz communications,” *IEEE Wireless Commun. Lett.*, vol. 10, no. 6, pp. 1256–1260, Jun. 2021.
- [11] Q. Zhang, Y.-C. Liang, and H. V. Poor, “Reconfigurable intelligent surface assisted MIMO symbiotic radio networks,” *IEEE Trans. Commun.*, vol. 69, no. 7, pp. 4832–4846, Jul. 2021.
- [12] A. D. J. Torres *et al.*, “Near and far-field communications with large intelligent surfaces,” in *Proc. Asilomar Conf. Signals, Syst. Comput.*, Pacific Grove, CA, USA, Nov. 2020, pp. 564–568.
- [13] M. D. Renzo *et al.*, “Reconfigurable intelligent surface vs. relaying: Difference, similarities, and performance comparison,” *IEEE Open J. Commun. Soc.*, vol. 1, pp. 798–807, 2020.

- [14] E. Björnson, O. Özdogan, and E. G. Larsson, "Intelligent reflecting surface versus decode-and-forward: How large surfaces are needed to beat relaying?" *IEEE Wireless Commun. Lett.*, vol. 9, no. 2, pp. 244–248, Feb. 2020.
- [15] W. Tang *et al.*, "Wireless communications with programmable metasurface: New paradigms, opportunities, and challenges on transceiver design," *IEEE Wireless Commun.*, vol. 27, no. 2, pp. 180–187, Apr. 2020.
- [16] E. Basar, "Reconfigurable intelligent surface-based index modulation: A new beyond MIMO paradigm for 6G," *IEEE Trans. Commun.*, vol. 68, no. 5, pp. 3187–3196, May 2020.
- [17] C. Huang, R. Mo, and Y. Yuen, "Reconfigurable intelligent surface assisted multiuser MISO systems exploiting deep reinforcement learning," *IEEE J. Sel. Areas Commun.*, vol. 38, no. 8, pp. 1839–1850, Jun. 2020.
- [18] O. Özdogan, E. Björnson, and E. G. Larsson, "Intelligent reflecting surfaces: Physics, propagation, and pathloss modeling," *IEEE Wireless Commun. Lett.*, vol. 9, no. 5, pp. 581–585, May 2020.
- [19] F. H. Danufane, M. D. Renzo, J. de Rosny, and S. Tretyakov, "On the path-loss of reconfigurable intelligent surfaces: An approach based on Green's theorem applied to vector fields," *IEEE Trans. Commun.*, vol. 69, no. 8, pp. 5573–5592, Aug. 2021.
- [20] J. C. B. Garcia, A. Sibille, and M. Kamoun, "Reconfigurable intelligent surfaces: Bridging the gap between scattering and reflection," *IEEE J. Sel. Areas Commun.*, vol. 38, no. 11, pp. 2538–2547, Nov. 2020.
- [21] W. Tang *et al.*, "Wireless communications with reconfigurable intelligent surface: Path loss modeling and experimental measurement," *IEEE Trans. Wireless Commun.*, vol. 20, no. 1, pp. 421–439, Jan. 2021.
- [22] E. Björnson and L. Sanguinetti, "Rayleigh fading modeling and channel hardening for reconfigurable intelligent surfaces," *IEEE Wireless Commun. Lett.*, vol. 10, no. 4, pp. 830–834, Apr. 2021.
- [23] M. Najafi, V. Jamali, R. Schober, and H. V. Poor, "Physics-based modeling and scalable optimization of large intelligent reflecting surfaces," *IEEE Trans. Commun.*, vol. 69, no. 4, pp. 2673–2691, Apr. 2021.
- [24] E. Basar *et al.*, "Indoor and outdoor physical channel modeling and efficient positioning for reconfigurable intelligent surfaces in mmWave bands," *IEEE Trans. Commun.*, early access, Sep. 20, 2021, doi: [10.1109/TCOMM.2021.3113954](https://doi.org/10.1109/TCOMM.2021.3113954).
- [25] E. Basar and I. Yildirim, "Reconfigurable intelligent surfaces for future wireless networks: A channel modeling perspective," *IEEE Wireless Commun.*, vol. 28, no. 3, pp. 108–114, Jun. 2021.
- [26] Y. Sun *et al.*, "A 3D non-stationary channel model for 6G wireless systems employing intelligent reflecting surface," in *Proc. IEEE WCSP*, Nanjing, China, Oct. 2020, pp. 19–25.
- [27] A. Goldsmith, *Wireless Communication*, Cambridge, U.K.: Cambridge Univ. Press, 2005.
- [28] N. Yu *et al.*, "Light propagation with phase discontinuities: Generalized laws of reflection and refraction," *Science*, vol. 334, no. 6054, pp. 333–337, Oct. 2011.
- [29] S. Saunders and A. Aragon-zavala, *Antennas and Propagation for Wireless Communication Systems*, 2nd ed. West Sussex, U.K.: Wiley, 2007.
- [30] H. Jiang, Z. Zhang, L. Wu, J. Dang, and G. Gui, "A 3-D non-stationary wideband geometry-based channel model for MIMO vehicle-to-vehicle communications in tunnel environments," *IEEE Trans. Veh. Technol.*, vol. 68, no. 7, pp. 6257–6271, Jul. 2019.
- [31] S. Zeng, H. Zhang, B. Di, Z. Han, and L. Song, "Reconfigurable intelligent surface (RIS) assisted wireless coverage extension: RIS orientation and location optimization," *IEEE Commun. Lett.*, vol. 25, no. 1, pp. 269–273, Jan. 2021.
- [32] R. He, B. Ai, G. L. Stüber, G. Wang, and Z. Zhong, "Geometrical-based modeling for millimeter-wave MIMO mobile-to-mobile channels," *IEEE Trans. Veh. Technol.*, vol. 67, no. 4, pp. 2848–2863, Apr. 2018.
- [33] A. Zajic, *Mobile-to-Mobile Wireless Channels*, Norwood, MA, USA: Artech House, 2012.
- [34] Y. Yuan, C.-X. Wang, Y. He, M. M. Alwakeel, and E. M. Aggoune, "3D wideband non-stationary geometry-based stochastic models for non-isotropic MIMO vehicle-to-vehicle channels," *IEEE Trans. Wireless Commun.*, vol. 14, no. 12, pp. 6883–6895, Dec. 2015.
- [35] H. Jiang, Z. Zhang, J. Dang, and L. Wu, "A novel 3-D massive MIMO channel model for vehicle-to-vehicle communication environments," *IEEE Trans. Commun.*, vol. 66, no. 1, pp. 79–90, Jan. 2018.
- [36] M. Yang, B. Ai, R. He, L. Chen, X. Li, J. Li, B. Zhang, C. Huang, and Z. Zhong, "A cluster-based three-dimensional channel model for vehicle-to-vehicle communications," *IEEE Trans. Veh. Technol.*, vol. 68, no. 6, pp. 5208–5220, Jun. 2019.
- [37] *Technical Specification Group Radio Access Network: Study on Channel model for frequencies from 0.5 to 100 GHz (Release 16)*, document TR 38.901, v16.1.0, 3GPP, Dec. 2019.
- [38] S. Wu, C.-X. Wang, M. Aggoune, M. M. Alwakeel, and Y. He, "A non-stationary 3-D wideband twin-cluster model for 5G massive MIMO channels," *IEEE J. Sel. Areas Commun.*, vol. 32, no. 6, pp. 1207–1218, Jun. 2014.
- [39] J. Bian *et al.*, "A WINNER+ based 3-D non-stationary wideband MIMO channel model," *IEEE Trans. Wireless Commun.*, vol. 17, no. 3, pp. 1755–1767, Mar. 2018.
- [40] C. F. López and C.-X. Wang, "Novel 3-D non-stationary wideband models for massive MIMO channels," *IEEE Trans. Wireless Commun.*, vol. 17, no. 5, pp. 2893–2905, May 2018.
- [41] B. Xiong, Z. Zhang, J. Zhang, H. Jiang, J. Dang, and L. Wu, "Novel multi-mobility V2X channel model in the presence of randomly moving clusters," *IEEE Trans. Wireless Commun.*, vol. 20, no. 5, pp. 3180–3195, May 2021.
- [42] S. Wu, C.-X. Wang, E.-H. M. Aggoune, M. M. Alwakeel, and X. You, "A general 3-D non-stationary 5G wireless channel model," *IEEE Trans. Commun.*, vol. 66, no. 7, pp. 3065–3078, Jul. 2018.
- [43] H. Jiang *et al.*, "A general wideband non-stationary stochastic channel model for intelligent reflecting surface-assisted MIMO communications," *IEEE Trans. Wireless Commun.*, vol. 20, no. 8, pp. 5314–5328, Aug. 2021.
- [44] M. A. ElMossallamy *et al.*, "Reconfigurable intelligent surface for wireless communications: Principles, challenges, and opportunities," *IEEE Trans. Cognit. Commun. Netw.*, vol. 6, no. 3, pp. 990–1002, Sep. 2020.
- [45] B. Matthiesen, E. Björnson, E. De Carvalho, and P. Popovski, "Intelligent reflecting surface operation under predictable receiver mobility: A continuous time propagation model," *IEEE Wireless Commun. Lett.*, vol. 10, no. 2, pp. 216–220, Feb. 2021.



Baiping Xiong received the B.Eng. degree in information engineering from Southeast University, Nanjing, China, in 2019, where he is currently pursuing the Ph.D. degree with the National Mobile Communications Research Laboratory.



Zaichen Zhang (Senior Member, IEEE) was born in Nanjing, China, in 1975. He received the B.S. and M.S. degrees in electrical and information engineering from Southeast University, Nanjing, in 1996 and 1999, respectively, and the Ph.D. degree in electrical and electronic engineering from The University of Hong Kong, Hong Kong, in 2002. From 2002 to 2004, he was a Post-Doctoral Fellow with the National Mobile Communications Research Laboratory, Southeast University. He joined the School of Information Science and Engineering, Southeast University, in 2004, where he is currently a Professor. He has published more than 200 articles and issued 50 patents. His current research interests include 6G mobile communication systems, optical wireless communications, and quantum information processing.



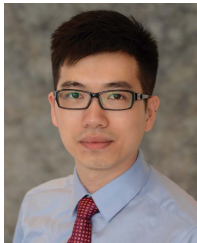
Hao Jiang (Member, IEEE) received the B.S. and M.S. degrees in electrical and information engineering from the Nanjing University of Information Science and Technology, Nanjing, China, in 2012 and 2015, respectively, and the Ph.D. degree from Southeast University, Nanjing, in 2019. From 2017 to 2018, he was a Visiting Student with the Department of Electrical Engineering, Columbia University, New York, NY, USA. His current research interests include in the general area of wireless channel measurements and modeling, B5G wireless communication networks, signal processing, machine learning, and AI-driven technologies.



Hongming Zhang (Member, IEEE) received the B.Eng. degree (Hons.) in telecommunications from the Nanjing University of Aeronautics and Astronautics (NUAA) and the City University of London, in 2011, and the M.Sc. and Ph.D. degrees in wireless communications from the University of Southampton in 2012 and 2017, respectively. From 2017 to 2018, he was with the Department of Electrical Engineering, Columbia University, New York, NY, USA. He is currently an Assistant Professor with the School of Information and Communication Engineering, Beijing University of Posts and Telecommunications, Beijing, China. His research interests include wireless communications, heterogeneous network performance analysis and optimization, and machine learning.



Liang Wu (Senior Member, IEEE) received the B.S., M.S., and Ph.D. degrees from the School of Information Science and Engineering, Southeast University, Nanjing, China, in 2007, 2010, and 2013, respectively. From September 2011 to March 2013, he was with the School of Electrical Engineering and Computer Science, Oregon State University, as a Visiting Ph.D. Student. In September 2013, he joined the National Mobile Communications Research Laboratory, Southeast University, where he has been an Associate Professor, since April 2018. His research interests include optical wireless communications, multiple input and multiple output technology, interference alignment, and wireless indoor localization.



Jiangfan Zhang (Member, IEEE) received the B.Eng. degree in communication engineering from the Huazhong University of Science and Technology, Wuhan, China, in 2008, the M.Eng. degree in information and communication engineering from Zhejiang University, Hangzhou, China, 2011, and the Ph.D. degree in electrical engineering from Lehigh University, Bethlehem, PA, USA, in 2016. From 2016 to 2018, he was a Post-Doctoral Research Scientist with the Department of Electrical Engineering, Columbia University, New York, NY, USA.

Since 2018, he has been with the Department of Electrical and Computer Engineering, Missouri University of Science and Technology, Rolla, MO, USA, where he is currently an Assistant Professor. His research interests include signal processing, machine learning, and their applications to cybersecurity, cyber-physical systems, the Internet of Things, smart grids, and sonar processing. He was a recipient of the Dean's Doctoral Student Assistantship, a Gotshall Fellowship, and a P. C. Rossin Doctoral Fellow at Lehigh University.



Jian Dang (Senior Member, IEEE) received the B.S. degree in information engineering and the Ph.D. degree in information and communications engineering from Southeast University, Nanjing, China, in July 2007 and September 2013, respectively. From September 2010 to March 2012, he was with the Department of Electrical and Computer Engineering, University of Florida, Gainesville, FL, USA, as a Visiting Scholar. Since September 2013, he has been with the National Mobile Communications Research Laboratory, Southeast University. He is currently an Associate Professor. His research interests include signal processing in wireless communications and optical mobile communications.